Journal of Physics Communications

OPEN ACCESS

RECEIVED
10 October 2019

REVISED
14 January 2020

ACCEPTED FOR PUBLICATION
16 January 2020

PUBLISHED
4 February 2020

PAPER

Topological analysis of pattern formation in cooling granular gases confined by elastic wall

Ryosuke Yano[1] **and Minkyu Kim**[2]

[1] Tokio Marine & Nichido Risk Consulting Co. ltd., 100-0004, 1-5-1, Otemachi, Chiyoda-ku, Tokyo, 100-0004, Japan
[2] Graduate School of Mathematical Sciences, University of Tokyo, 153-0041, 3-8-1, Komaba, Meguro-ku, Tokyo, Japan

E-mail: kim@ms.u-tokyo.ac.jp

Keywords: topological analysis, pattern formation, granular gases, persistent homology

Abstract

In this paper, we investigate the topological characteristics of the pattern formation in the cooling granular gases confined by the elastic wall. The persistent homology and Voronoi's analysis and its derivative analyses are applied to accomplish our aim. The growth of the pattern formation can be identified by the switch between the logarithmic concave and logarithmic convex in the life-span-distribution obtained using the persistence diagram. Furthermore, three phases are identified by the zeroth or first order Betti number, when a form of the wall is the square. Finally, the characteristics of the coordination of granular particles condensing around the elastic wall are investigated by the Voronoi's analysis, bond-angle analysis, and polyhedral template matching. We confirm that some clusters of the granular particles condensing around the elastic spherical-wall certainly attribute to their crystallization categorized as the typical coordination.

1. Introduction

The accurate classification of the phase of matter [1] is significant to characterize the physical property of matter such as solid (crystal structure), liquid, or gases. Meanwhile, such a classification of the phase of matter sometimes involves difficulties as observed in the classification of the phase of glass [2]. For example, we are still unable to answer to the question whether glass corresponds to the liquid, solid or glassy state. The topological characterization of the phase of matter on the basis of locations of atoms or particles has been used in order to overcome such difficulties involved with the specification of the phase of matter. For example, the topological characterization of the crystal has been widely used, as represented by the Voronoi's analysis (VA) using coordination of atoms [3]. On the other hand, the specification of the coordination of atoms (particles) from their locations becomes difficult, when thermal fluctuations of atoms (particles) become significant. Therefore, the specification of the coordination of thermal fluctuating particles involves difficulties even with the VA. Meanwhile, the recent application of the persistent homology (PH) [4] to numerical data (i.e., locations of atoms) of glass by Hiraoka *et al* [5] succeeded the discrimination of the glassy state from the liquid state, where the coordination of atoms in glass seems to be random, because thermal fluctuations are significant at glance. Then, the PH enables us to find the ordered structure even under the marked thermal fluctuations. The analogy between glass and granular matter is sometimes indicated by the fact that sheared granular media forms the disordered glassy state via the jamming transition [6]. In previous studies of the dense granular packing [7], the characteristics of the force-chain-network was analyzed by the PH, whereas the crystal characteristics of the densely packed granular particles was investigated by the VA.

As a peculiar characteristics of the dilute granular gases, the cluster formation from the initially homogeneous cooling state (HCS) [8, 9] has been well studied by Brey [10] and his coworkers, whereas the characteristics of the HCS of the granular gases has been studied in detail by Santos [11], Brilliantov [8] and their coworkers or Yano [12]. The mode-analysis [8, 10] of the hydrodynamics equation of the granular gases can demonstrate such an instability of the HCS, which attributes to the pattern formation via aggregations (clusters) of the granular particles. Of course, the granular gases correspond to the status, in which the volume fraction of

the granular particles is low, adequately, and thermal motions of granular particles are significant. Actually, the phase of granular matter easily changes in accordance with $\rho L r_d^2$ (ρ: density, L: representative length, r_d: diameter of sphere) and restitution coefficient, as demonstrated by Esipov and Pöschel [13]. The primary aim of our present study is to answer to the question whether the transition from the HCS to the pattern formation of the granular gases can be demonstrated by the PH or VA or its derivative analyses, namely, bond-angle analysis (BAA) [14] and polyhedral template matching (PTM) [15]. Additionally, we investigate the crystal structure of granular particles, which condensate around the wall, using the VA, BAA and PTM. Here, the topological phase-transition corresponds to the specific change in topological characteristics, then, we must remind that the topological phase never be same as the physical phase (gases, liquid, or solid).

Now, we consider the granular gases confined by the *elastic wall*, with which all the granular particles collide elastically. The reason why we consider the elastic (heating) wall [16] is to exclude both excessive accumulation of granular particles around the wall owing to their inelastic collisions with the wall [17] and long range-correlations among granular particles owing to the use of the periodic boundary, which is unfavorable in the PH analysis. The time-evolution of the granular particles with the constant restitution coefficient and smooth surface is calculated by the event-driven (ED) method [17].

This paper is organized as follows. Firstly, the preliminaries for the Betti number [18], persistence diagram (PD) [19], or VA, BAA and PTM are demonstrated together with the ED method in section 2, briefly. Afterwards, the changes in the PD and Betti number in accordance with the time-evolution of the granular particles are discussed in order to confirm whether they are able to capture the transition from the HCS to the pattern formation or not, in section 3. Next, the BAA, VA, and PTM are applied to numerical results of the granular gases confined by the spherical (SP) boundary in order to confirm whether the tendency of the pattern formation of granular gases from the HCS can be identified by the BAA, VA, and PTM or not, in section 4. Additionally, we investigate which coordination the granular particles, which condensate around the elastic wall densely, are categorized as. Finally, we make concluding remarks in section 5.

2. Preliminaries in topological context

Before stating our discussions of numerical results, the following items are demonstrated to help readers' understanding of the mathematical definitions and terminologies used in topological contexts and numerical simulation.

A. Betti number

B. Persistence diagram (PD)

C. From point could data to PD

D. VA, BAA and PTM

E. Event Driven (ED) method to simulate granular particles

2.1. Betti number

For a non-negative integer p, the *p-th Betti number* of simplicial complexes (see its definition in appendix A) is one of classical topological invariants [20]. It is the number assigned to each simplicial complex, which implies information about its topology. The Betti number implies a 'persistence' with respect to 'continuous deformations'. In other words, the Betti number is invariant under 'continuous deformations'. We note that the Betti number does not imply geometric information (volume, metric etc.) of simplicial complexes. Informally speaking, the p-th Betti number of a simplicial complex X is a number of 'p-dimensional holes' of X. We give the heuristic explanation of the Betti number using figure 1. The simplicial complex in figure 1 consists of '7' vertices and '8' edges.

A vertex is called as 0-simplex, and an edge is called as 1-simplex from the simplicial point of view. The simplicial complex in figure 1 has no higher-dimensional simplex such as the face. Now, we compute the 0th Betti number. 0-dimensional hole stands for the *connected component* following conventions. In short, the 0th Betti number counts the number of connected components. Since the simplicial complex in in figure 1 has one connected component, its 0th Betti number is '1'. On the other hand, a 1-dimensional hole means a circular hole. The simplicial complex in figure 1 has two circular holes along with the hexagon part and the square part. Hence, the 1st Betti number is '2'. These observations can be generalized to the case $p \geqslant 2$. For example, we interpret 2-dimensional hole as a balloon-like hole or *2-sphere*-like hole. We introduce the notion of homology in order to deal with such 'p-dimensional holes' in a formal way.

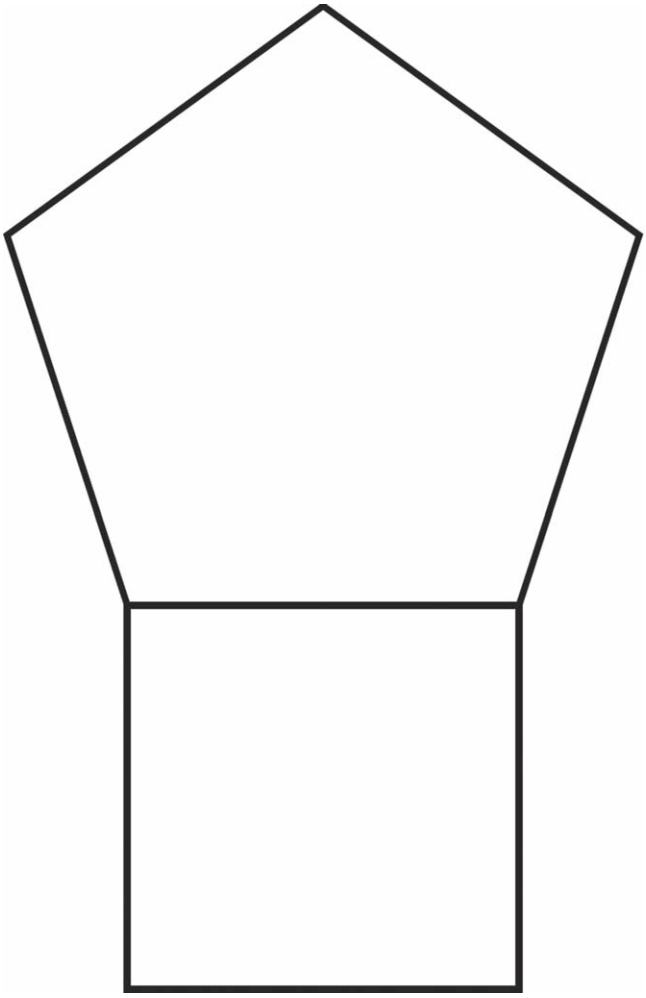

Figure 1. An example of a simplicial complex.

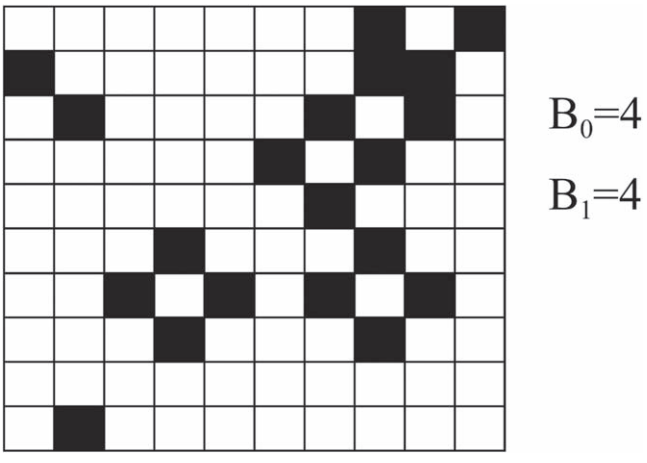

Figure 2. Schematic of calculation of B_0 and B_1 in 10 × 10 pixels with monotone PNG file by CHomP [21].

Betti number on the basis of locations of granular particles is calculated using the monotone PNG format with the CHomP [21]. Figure 2 shows the zeroth and first order Betti numbers, which are calculated using monotone PNG. We can readily understand that both B_0 (connection) and B_1 (hole) are equal to '4', as shown in figure 2.

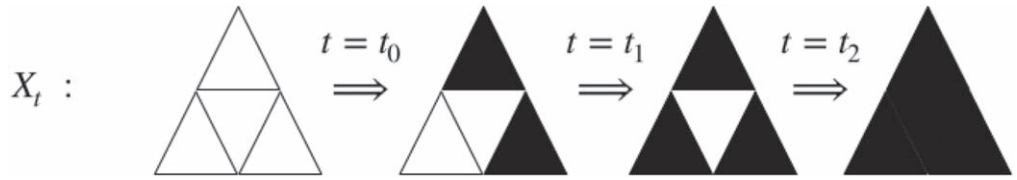

Figure 3. An example of a filtration of a simplicial complex.

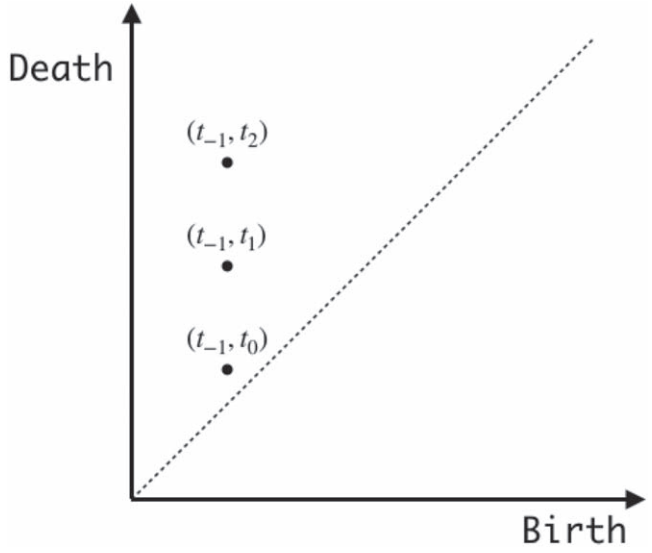

Figure 4. The PD of the filtration in figure 3.

2.2. Persistence diagram (PD)

For a nonnegative integer p, the p-th Betti number counts 'p-dimensional holes' of a simplicial complex, as we explain in section 2.1. A *persistence diagram* (PD) is a diagram, which records *birth and death* of 'p-dimensional holes', i.e. we consider 'time-evolution' of a simplicial complex and are interested in the change of its topology.

The time-evolution, formally speaking, corresponds to *filtration* of a simplicial complex. A filtration of a simplicial complex X is given by a sequence $\{X_t\}_{t\in\mathbb{R}}$ of simplicial sub-complexes $X_t \subset X$ parametrized by $t \in \mathbb{R}$ such that

- $X_{t_0} \subset X_{t_1}$ for $t_0 < t_1$.
- $\bigcup_t X_t = X$ and $\bigcap_t X_t = \varnothing$.

A filtration can be understood as a movie film which records how a simplicial complex grows as time evolves. We give an example in figure 3; the filtration $\{X_t\}_{t\in\mathbb{R}}$ is an empty complex for sufficiently small t, say $t = t_{-1}$; the filtration $\{X_t\}_{t\in\mathbb{R}}$ is constant except for $t = t_0, t_1, t_2$, where it grows up, as shown in figure 3. The *p-th PD* of a filtration $\{X_t\}_{t\in\mathbb{R}}$ is induced by the data of when the p-dimensional holes are born and dead as time evolves. Informally speaking, for a p-dimensional hole h of some X_t, we mark a point $(b_h,\ d_h)$ on xy-plane where $b_h \in \mathbb{R}$ ($d_h \in \mathbb{R}$, resp.) is the time when the hole h is born (dead, resp.).

The p-th PD is obtained by plotting such $(b_h,\ d_h)$. The PD is given by multiple set in general since there is a possibility that some holes have the same birth time and death time. We give an example of the PD in figure 4, which is obtained from the filtration in figure 3. Note that the point $(t_{-1},\ t_0)$ in the PD has multiplicity of '2'. There is an obvious problem with respect to the definition of such a hole h in the time-evolution. The notion of *persistent homology* and some decomposition theorems are necessary to define PDs in a formal way. Their brief overview is given in appendix C.

2.3. From point cloud data to PD

In this subsection, an overview about how the PD is obtained from point cloud data is given. Since the PD is obtained from a filtration of a simplicial complex, it suffices to construct a filtration of a simplicial complex

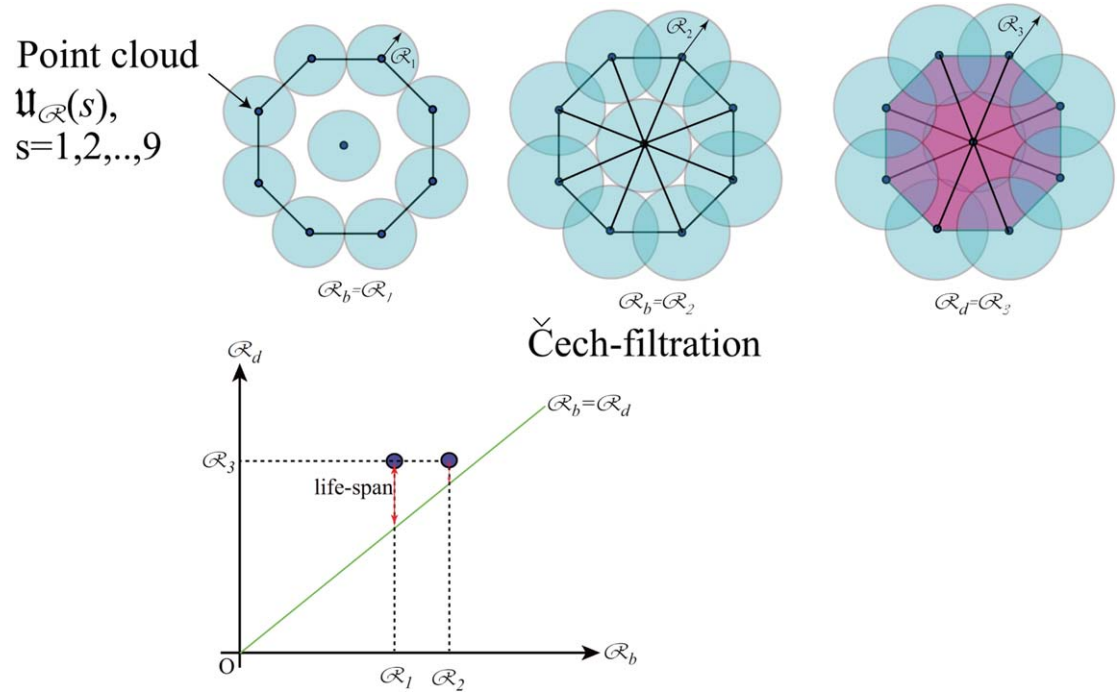

Figure 5. $\mathfrak{U}_{\mathscr{R}}$ of nine point cloud ($s = 1, 2, .., 9$), when $\mathscr{R} = \mathscr{R}_1$ (upper-left frame), $\mathscr{R} = \mathscr{R}_2$ (upper-middle frame) and $\mathscr{R} = \mathscr{R}_3$ (upper-right frame) in Čech filtration. PD obtained by birth-death of holes corresponding to above three frames (lower frame).

starting from point cloud data. In practice, a point cloud data is usually given by a finite set S in a Euclidean space $\mathbb{R}^N$. For a positive number $\mathscr{R}$, an open covering of S in $\mathbb{R}^N$ given by $\mathfrak{U}_{\mathscr{R}} = \{\mathscr{B}_{\mathscr{R}}(s)\}_{s\in S}$ is considered.

Here, $\mathscr{B}_{\mathscr{R}}(s)$ is the $\mathscr{R}$-neighborhood of a point $s \in S$ with a radius of $\mathscr{R}$. There are several ways to construct a cell complex from the open covering $\mathfrak{U}_{\mathscr{R}}$: the Čech complex, the Alpha complex, the Vietoris-Rips complex, etc [20, 22, 23].

If we denote one of such complexes by $C_{\mathscr{R}}$, then, $\{C_{\mathscr{R}}\}_{\mathscr{R}>0}$ gives a filtration of a cell complex where we consider $\mathscr{R}$ as time, i.e. $C_{\mathscr{R}_0} \subset C_{\mathscr{R}_1}$ for $0 < \mathscr{R}_0 < \mathscr{R}_1$. the PD is obtained from the filtration $\{C_{\mathscr{R}}\}_{\mathscr{R}>0}$. We note that the PD is determined by the point cloud data S in $\mathbb{R}^N$.

Figure 5 shows growths of $\mathfrak{U}_{\mathscr{R}}$ of eight point cloud by enlarging $\mathscr{R}$. The upper-left frame of figure 5 shows the birth of the hole, when $\mathscr{R} = \mathscr{R}_1$. The upper-middle frame of figure 5 shows births of eight holes, when $\mathscr{R} = \mathscr{R}_2$. The upper-right frame of figure 5 shows deaths of holes, when $\mathscr{R} = \mathscr{R}_3$. Consequently, the PD of these birth-death-sets of holes ($\mathscr{R}_b$, $\mathscr{R}_d$) are shown in lower-frame of figure 5, in which $\mathscr{R}_b$ and $\mathscr{R}_d$ correspond to the radius of $\mathscr{B}_{\mathscr{R}}$ (i.e., $\mathscr{R}$), which yields the birth and death, respectively. Of course, eight-fold-points are plotted on $(\mathscr{R}_b, \mathscr{R}_d) = (\mathscr{R}_2, \mathscr{R}_3)$ owing to the birth-death of eight holes.

2.4. VA, BAA and PTM

The Voronoi's analysis (VA), bond-angle-analysis (BAA) and polyhedral template matching (PTM) have been used to analyze the structure of the crystal on the basis of coordination of atoms. In particular, the analytical tools are freely provided by the codes of Voro++ [24] and Vorotop [25] in Ovito [26]. Then, we can utilize such analyzers in order to analyze the crystal structures of granular particles. Of course, the crystal structure usually postulates the densely packed status of granular particles, where thermal fluctuations of atoms are negligible. We, however, focus on the crystal characteristics, before and after granular particles are densely condensed around the wall owing to their markedly low kinetic energy. Here, schematics of the VA, BAA and PTM are demonstrated, briefly.

In order to discuss the VA, BAA and PTM, we start our discussion by mentioning to the Voronoi's diagram (VD).

$\mathbb{E}$ is space such as $\mathbb{E} \subseteq \mathbb{R}^n$ ($n \in \mathbb{N}$). Let's think elements $\boldsymbol{g}_1, \boldsymbol{g}_2, \cdots \boldsymbol{g}_n \in \mathbb{E}$. Here, $\bigcup_{k=1}^{n} \boldsymbol{g}_k := \mathbb{G}$.

We define the distance between the point $\boldsymbol{P} \in \mathbb{E}$ and $\boldsymbol{g}_i$ as

$$d(\boldsymbol{P}, \boldsymbol{g}_i),$$

Then, the Voronoi's domain $R(\mathbb{G}; \boldsymbol{g}_i)$ is defined by:

$$R(\mathbb{G}; \boldsymbol{g}_i) := \{\boldsymbol{P} \in \mathbb{E} | d(\boldsymbol{P}, \boldsymbol{g}_i) < d(\boldsymbol{P}, \boldsymbol{g}_j),\ j \neq i\}, \tag{1}$$

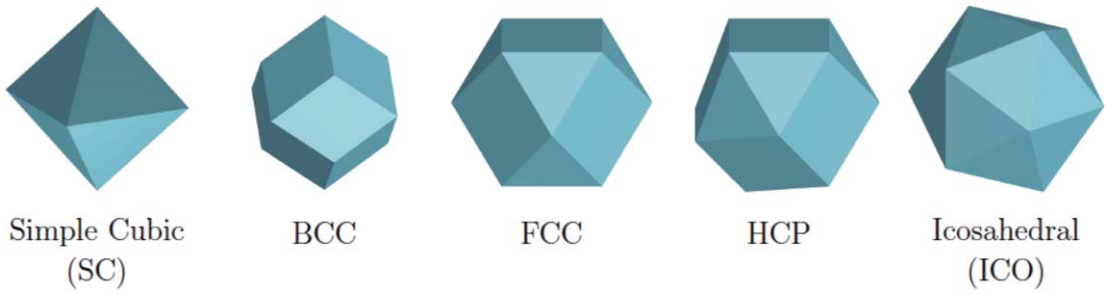

Figure 6. Schematic of convex hulls of SC, BCC, FCC, HCP and ICO used in PTM [15].

From equation (1), $\mathbb{E}$ is divided into $R(\mathbb{G},\ \boldsymbol{g}_i)$ $(i \in [1,\ n] \cap \mathbb{N})$. We call these divided structures of $\mathbb{E}$ by $R(\mathbb{G},\ \boldsymbol{g}_i)$ as the VD.

The VD is described by the Delaunay tetrahedralization in the case of $\mathbb{E} \subseteq \mathbb{R}^3$. The significant problem in the VA is classifications of the VD using the typical crystal-coordination such as the face-centered-cubic (FCC), body-centered-cubic (BCC), hexagonal close-packed (HCP), icosahedral (ICO) and hybrid of FCC and HCP (FCC-HCP). The VA by Voro++ applies Weinberg's algorithm [27] to find the most appropriate crystal-coordination among the FCC, BCC, ICO, FCC-HCP and Other from the VD, in which *Other* indicates the status of coordination of granular particles, from which any crystal structure is not specified with the FCC, BCC, ICO and FCC-HCP.

Of course, there are other methods in order to categorize the crystal structure such as the Common Neighbor Analysis (CNA) [28], PTM [15], BAA [14] other than the VA. The PTM was proposed by Larsen-Schmidt-Schiøtz [15]. In the PTM, the similarity between two diagrams is evaluated by the Root-Mean-Square Deviation (RMSD), which is defined by [15]

$$\ell_{\mathrm{RMSD}}(\boldsymbol{v},\ \boldsymbol{w}) = \min_{s,\boldsymbol{Q}} \sqrt{\frac{1}{\aleph}\sum_{i=1}^{\aleph} ||s[\vec{v}_i - \bar{\boldsymbol{v}}] - (\boldsymbol{Q}[\vec{w}_i - \bar{\boldsymbol{w}}]^T)^T||_2^2}\,, \tag{2}$$

where $\boldsymbol{Q}$ is the right handed orthogonal matrix , $\bar{\boldsymbol{v}} = (1/\aleph)\sum_{i=1}^{\aleph} \vec{v}_i$, $\bar{\boldsymbol{w}} = (1/\aleph)\sum_{i=1}^{\aleph} \vec{w}_i$ are barycenter of $\boldsymbol{v}$ and $\boldsymbol{w}$. s is the optimal scaling of $\boldsymbol{v}$. The methods of findings of s and $\boldsymbol{Q}$ are proposed by Horn [29] and Theobald [30]. $\aleph$is the number of the neighboring atoms, and $\aleph = 6$ for the simple cubic (SC), 12 for the FCC, 12 for the HCP, 12 for the icosahedral (ICO) and 14 for the BCC are used. The detail of algorithm of the PTM is demonstrated by Larsen-Schmidt-Schiøtz [15]. Finally, we find the smallest RMSD among them which are calculated using the SC, FCC, HCP, ICO, and BCC. Additionally, *Other* corresponds to the state that any structure is not identified even with the SC, FCC, HCP, ICO, and BCC, when the minimum RMSD is larger than its critical value. Actually, $\boldsymbol{v}$ is the vector which indicates the vertex-set of the convex hull formed by N-neighboring atoms and $\boldsymbol{w}$ is the vector, which indicates the vertex-set of the convex hull of the reference templates, namely, the SC, FCC, HCP, ICO, and BCC (see figure 6 for convex-fulls of the SC, BCC, FCC, HCP and ICO). Hence, we can calculate the distribution of the RMSD ($f_{XX}(t,\ \ell_{\mathrm{RMSD}})$, $t \in \mathbb{R}_+$: time), when we specify the crystal structure of the atoms using two categories *Other* and *XX* (*XX* := SC, FCC, HCP, ICO and BCC). Finally, we mention to the BAA [14], briefly. The BAA was proposed by Ackland and Jones [14]. The BAA identifies the crystal structure of atom-i with the FCC, HCP, ICO, and BCC from angles (θ_{jik}) between two bonds ($\boldsymbol{r}_{ij}$ and $\boldsymbol{r}_{ik}$), which connect two sets of two neighboring atoms (i-j and i-k). The neighboring atoms are searched by the mean square distance of six neighboring atoms around the atom-i. Once the calculation of the angle between two bonds for several sets of two bonds is finished, functional of χ, which are calculated by angles θ_{jik}, identifies the crystal structure of atom-i with the FCC, HCP, ICO, BCC or *Other*.

2.5. Event-Driven method to simulate granular particles

The event-driven (ED) method has been frequently used in order to simulate a large number (N) of granular particles, whose simulation is difficult using the discrete element method (DEM), when the calculation of the $N(N-1)/2$ paired force-chain is beyond the computational resource. In particular, the ED method is suitable to simulate the dilute granular gases, in which the effects of deformations of contacting granular particles on the collective motion of all the granular particles are negligible.

The algorithm of the ED method is so simple. Provided that the k-th collision occurs at $t = t_k$ ($t_k \in \mathbb{R}_+$), we search for the occurrence-time of $k+1$-th collision, namely, t_{k+1}, which is calculated by

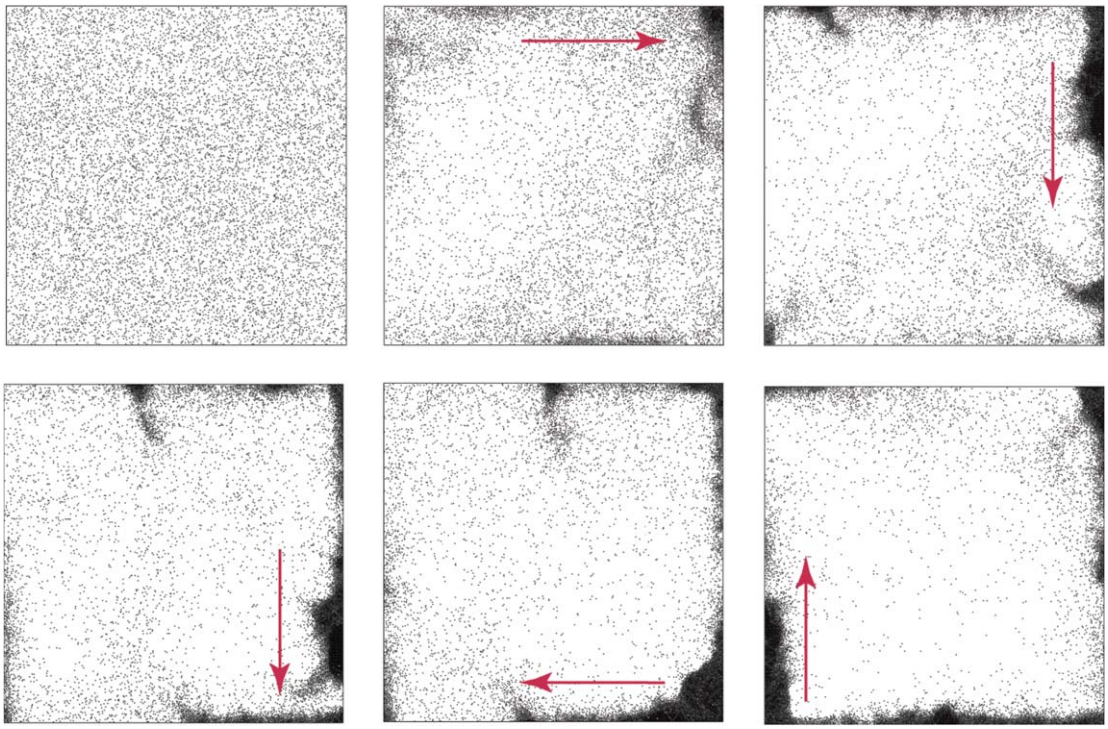

Figure 7. The time-evolutions of granular particles inside SQ boundary at $N_c = 0$ (upper-left frame), $0.1M$ (upper-middle frame), $11.25M$ (upper-right frame), $12.5M$ (lower-left frame), $13.75M$ (lower-middle frame) and $19.9M$ (lower-right frame), when $N = 10^4$.

$$
\begin{aligned}
&t_{k+1} \coloneqq t_k + \min\left(\Delta t_k^{ij}\right) \quad (i, j \in [1, 2, \ldots, N]),\\
&||\boldsymbol{x}_i(t_k + \Delta t_k^{ij}) - \boldsymbol{x}_j(\Delta t_k^{ij})|| = r_i + r_j,\\
&\boldsymbol{x}_i(t_k + \Delta t_k^{ij}) \coloneqq \boldsymbol{x}_i(t_k) + \boldsymbol{v}_i(t_k)\Delta t_k^{ij},
\end{aligned} \tag{3}
$$

where $\boldsymbol{x}_i(t) \in \mathbb{R}^d$ is the location of the granular particle indexed by i at t, $\boldsymbol{v}_i \in \mathbb{R}^d$ is the velocity of the i-th granular particle, r_i is the radius of the i-th granular particle.

Provided the boundary (wall) is considered, the occurrence-time of the collision between the granular particle and wall is calculated in a similar way to equation (3). Afterward, we compare the next collisional time calculated by two granular particles with that calculated by the granular particle and wall and select smaller t_{k+1} as next collisional time.

Once t_{k+1} is determined, we revise the locations of all the granular particles using $\boldsymbol{x}(t_{k+1}) = \boldsymbol{x}(t_k) + \boldsymbol{v}(t_k)\Delta t_k$ ($\Delta t_k \coloneqq t_{k+1} - t_k$). Finally, we revise the velocities of colliding granular particles or velocity of the granular particle colliding with the wall. Provided that the i-th and j-th granular particles collide, the velocities of colliding granular particles change at $t = t_{k+1}$ as follows:

$$
\begin{aligned}
\boldsymbol{v}_i(t_{k+1}) &= \boldsymbol{v}_i(t_k) - \frac{1+\epsilon}{2}(\boldsymbol{g}_{ij} \cdot \boldsymbol{n}_{ij})\boldsymbol{n}_{ij},\\
\boldsymbol{v}_j(t_{k+1}) &= \boldsymbol{v}_j(t_k) + \frac{1+\epsilon}{2}(\boldsymbol{g}_{ij} \cdot \boldsymbol{n}_{ij})\boldsymbol{n}_{ij},\\
\boldsymbol{g}_{ij} &= \boldsymbol{v}_i(t_k) - \boldsymbol{v}_j(t_k), \quad \boldsymbol{n}_{ij} = \frac{\boldsymbol{x}_i(t_k) - \boldsymbol{x}_j(t_k)}{||\boldsymbol{x}_i(t_k) - \boldsymbol{x}_j(t_k)||},
\end{aligned} \tag{4}
$$

where $\epsilon \in [0, 1]$ is the restitution coefficient, $\boldsymbol{g}_{ij}$ is the relative velocity and $\boldsymbol{n}_{ij} \in \Omega^2$ is the relative location-unit-vector.

The calculation of the velocity of the granular particle post-collision with the elastic wall is calculated in a similar way to equation (4) [17].

3. Persistent homology and their characteristics

In this section, we apply the PH to the cooling process of two dimensional granular gases confined by the elastic wall. Firstly, we investigate the PH of the granular discs in the case of the square (SQ) boundary. Next, we

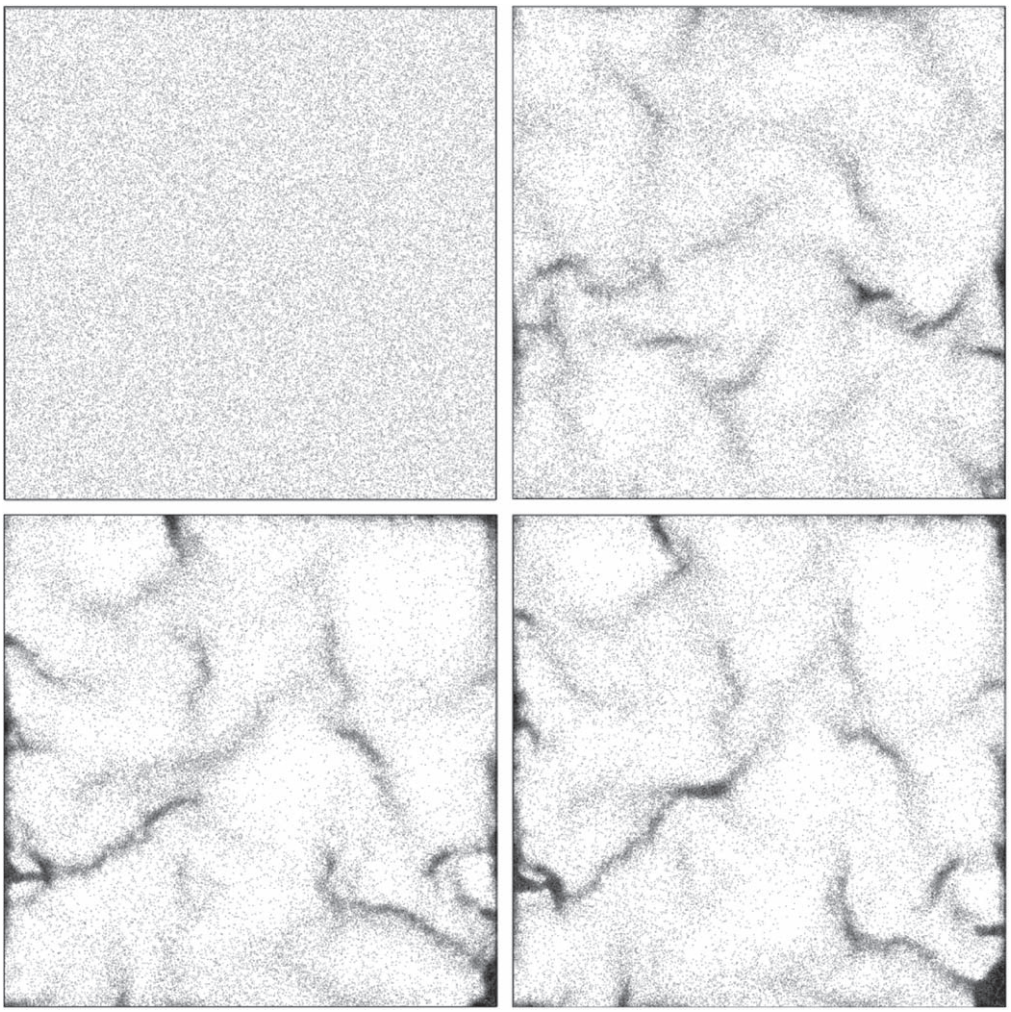

Figure 8. The time-evolutions of granular particles inside SQ boundary at $N_c = 0$ (upper-left frame), 2M (upper-right frame), 4M (lower-left frame) and 7.4M (lower-right frame), when $N = 5 \times 10^4$.

investigate the PH in the case of the circular (CI) boundary to consider the effects of form of the elastic wall on the PH. Finally, we investigate the PH of the granular spheres in the case of the spherical (SP) boundary.

3.1. Results in case of SQ boundary

The restitution coefficient of the granular discs is set as $\epsilon = 0.85$, and the volume fraction of the granular discs is fixed as $\phi = 7.85 \times 10^{-2}$. The length of one side of the square box (SQ boundary) is set as $L = 300$. Three types of the diameter of granular discs (r_d), namely, $r_d = 0.15, 0.21$ and 0.47 are considered. As a result, total number of granular discs (N) is set as $N = 10^4$ in the case of $r_d = 0.47$, $N = 5 \times 10^4$ in the case of $d = 0.21$ and $N = 10^5$ in the case of $r_d = 0.15$ owing to the constant volume fraction ($\phi = 7.85 \times 10^{-2}$). The initial velocities of the granular discs are randomly distributed in the range of $v_x \in [-1, 1]$, $v_y \in [-1, 1]$ and the initial positions of the granular discs are randomly distributed inside the elastic wall, namely, the range of $X \in [-0.5L, 0.5L]$ and $Y \in [-0.5L, 0.5L]$. The time-evolution of granular discs is calculated using the event-driven (ED) method [17], because the conventional molecular dynamics requires the vast calculation time, when forces between $N(N-2)/2$ paired granular discs are calculated.

Figures 7–9 show time-evolutions of the granular discs inside the SQ boundary at $N = 10^4, 5 \times 10^4$ and 10^5, respectively. Figure 7 indicates that some clusters are formed in the vicinity of the wall and the cluster with the maximum size rotates to clockwise direction along the wall. Such a rotation of granular discs along the wall is similar to the *emergence of the ordered collective-motion* in biological swarm inside the wall [31]. On the other hand, the granular particles tend to move away from the wall, when the heating wall with the constant temperature is used, as reported by Esipov and Pöschel [13]. The numerical results obtained using $N = 5 \times 10^4$ and 10^5 do not indicate such a rotation of the cluster with the maximum size, as shown in figures 8 and 9. Indeed, it is commonly observed in numerical results of $N = 10^4, 5 \times 10^4$ and 10^5 that the several small-clusters aggregate toward the larger clusters via their connections during the time-evolution. Of course, the elastic wall is

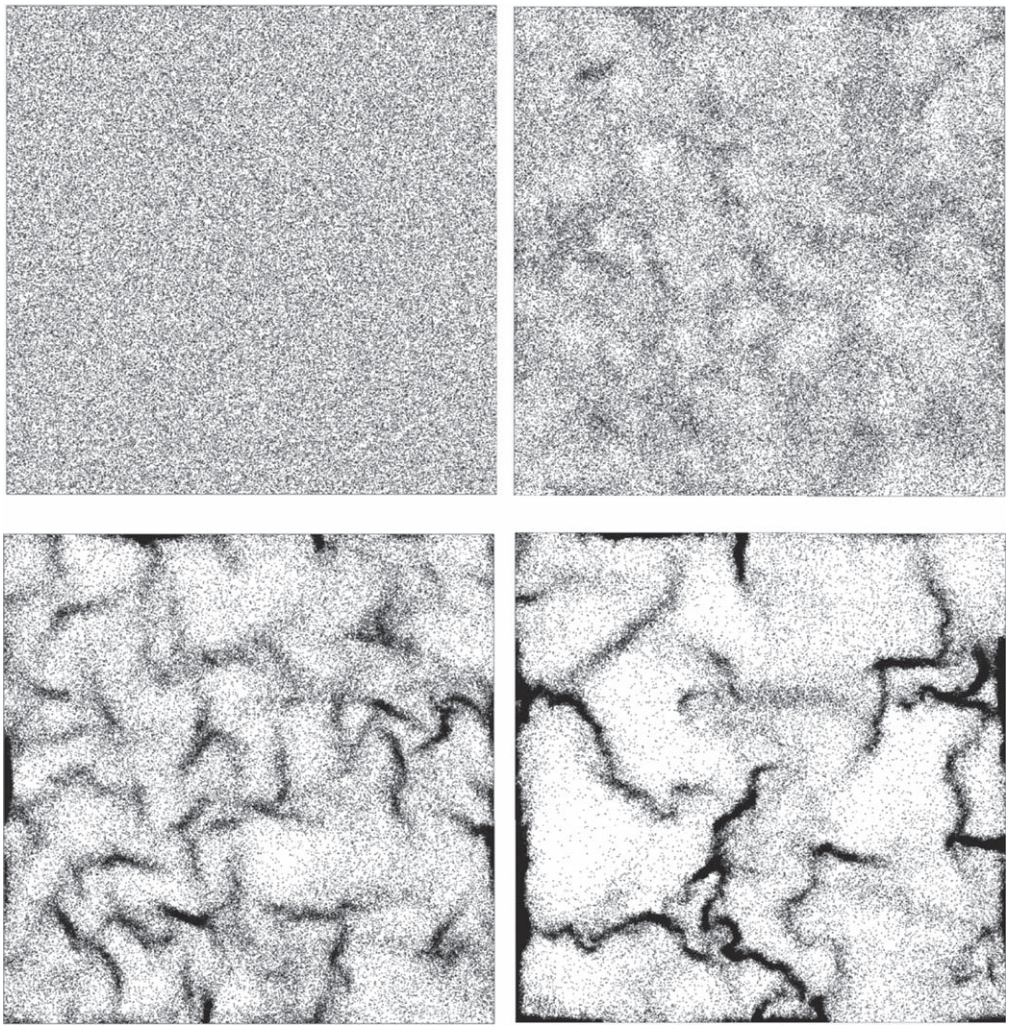

Figure 9. The time-evolutions of granular particles inside SQ boundary at $N_c = 0$ (upper-left frame), 2.15M (upper-right frame), 3.85M (lower-left frame) and 14.45M (lower-right frame), when $N = 10^5$.

a mathematical toy model to avoid the freeze of the calculation via the excessive accumulation of granular discs with the small kinetic energy in the vicinity of the wall and long range correlation of the granular discs owing to the use of the periodic boundary condition, which is unfavorable to topological analyses, because the distance between two granular discs in the PH must be modified by considering the periodicity at the boundary. The calculations of the PDs are performed using locations of the center of granular discs, namely, $(x_i,\ y_i)$ $(i \in [1,\ N] \cap \mathbb{N})$ and $\mathscr{R}$ (:radius of neighborhood (cover) $\mathscr{B}_{\mathscr{R}}(s_i)$ of point cloud S $(s_i \coloneqq (x_i,\ y_i) \in S)$). Therefore, we must remind that the *connection* in $d = 0$-persistent homology (d: dimension of PH) is not equivalent to the physical connections due to contacting granular discs. Reminding that the domain, which is occupied by neighborhood of i-th point-cloud, whose center is set as $(x_i,\ y_i)$, is expressed with $\mathscr{B}_{\mathscr{R}}(x_i,\ y_i)$, the connection between $\mathscr{B}_{\mathscr{R}}(x_i,\ y_i)$ and $\mathscr{B}_{\mathscr{R}}(x_j,\ y_j)$ is defined by $|\boldsymbol{x}_i - \boldsymbol{x}_j| < 2\mathscr{R}$ $(\boldsymbol{x}_i \coloneqq (x_i,\ y_i),\ 2\mathscr{R} > d)$. $\mathscr{R}$ is increased from zero to ∞, continuously in $\mathscr{R} \in \mathbb{R}_+$. $\mathscr{R} = \mathscr{R}_b$ is called as the *birth* of the hole, when the hole emerges when $\mathscr{R} = \mathscr{R}_b$, whereas $\mathscr{R} = \mathscr{R}_d$ is called as the *death* of the hole, when the hole disappears, when $\mathscr{R} = \mathscr{R}_d$. The plot of $(\mathscr{R}_b,\ \mathscr{R}_d)$ is called as the PD, as discussed in section 2.2. Additionally, $\ell \coloneqq \mathscr{R}_d - \mathscr{R}_b$ is called as the life-span of the hole, and defined by:

$$\ell \coloneqq \mathscr{R}_d - \mathscr{R}_b, \tag{5}$$

The image of the life-span (ℓ) is shown in the lower-frame of figure 5.

The open source program *homcloud* [32] is used to calculate the PD in our study. The PD is plotted using not $(\mathscr{R}_b,\ \mathscr{R}_d)$ but $(\mathscr{R}_b^2,\ \mathscr{R}_d^2)$ owing to the specification of the *homcloud*. Figure 10 shows PDs (left-half frames) and birth of holes with $\ell_{\max}$ (maximum value of ℓ) via connections of some of $\mathscr{B}_{\mathscr{R}}(s_i)$ $(i \in [1,\ N])$ at $N_c = 0, 2.15$M, 3.85M and 11.4M (right-half frames), when $N = 10^5$ (N_c: collision number, M: million), respectively. The color of the contour expresses the number of holes, which has $(\mathscr{R}_b^2,\ \mathscr{R}_d^2)$, where U $(\mathscr{R}_b^2,\ \mathscr{R}_d^2)$ is the square domain, whose center of gravity is $(\mathscr{R}_b^2,\ \mathscr{R}_d^2)$ and length of one side of the square is set as $\Delta \in \mathbb{R}_+$. Readers remind that

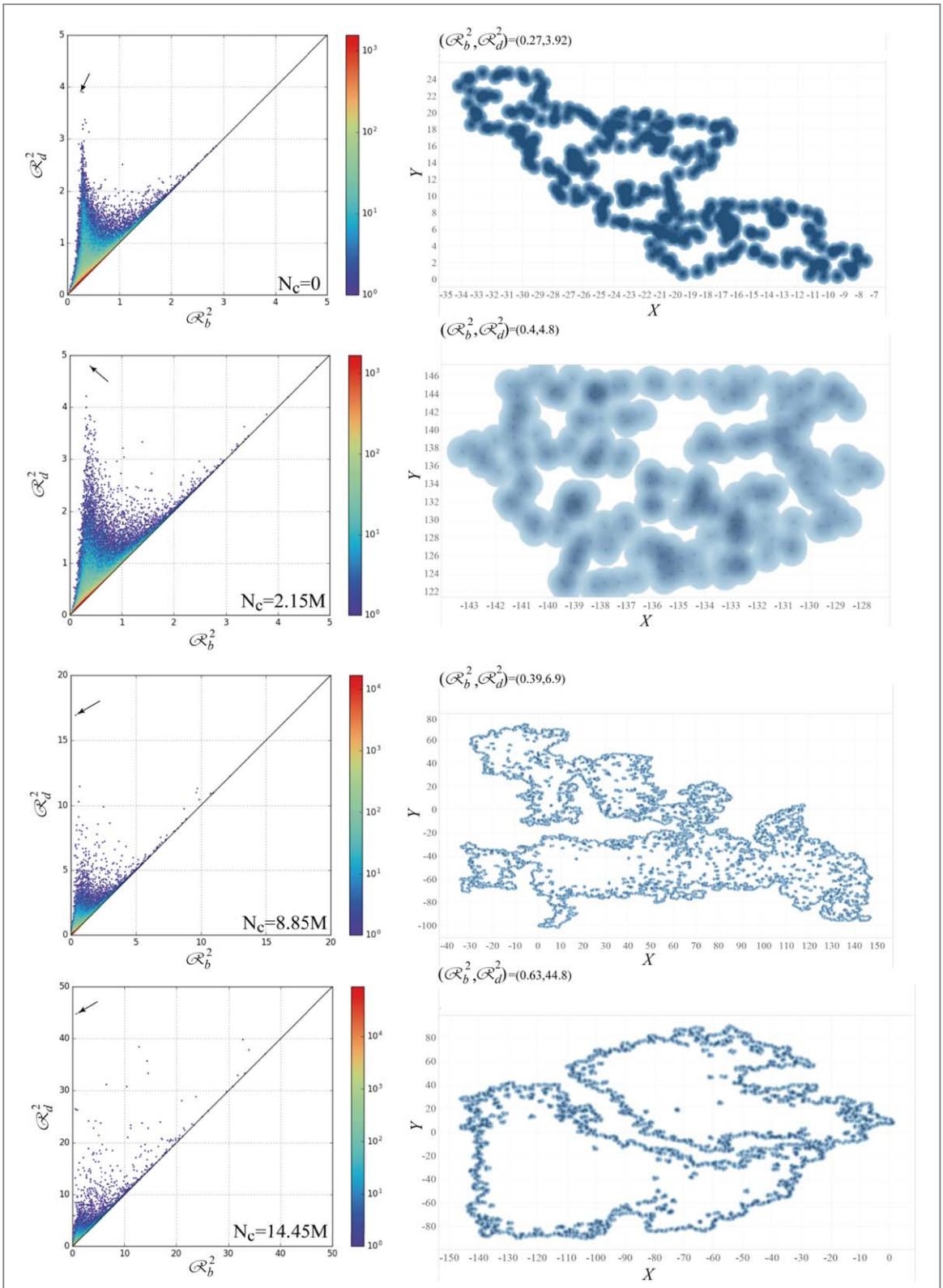

Figure 10. $d = 1$-PDs and their schematics of births of holes at $\ell_{\max}$ in cases of $N_c = 0$ (top-frame), $N_c = 2.15$M (2nd frame from the top), $N_c = 8.85$M (2nd frame from the bottom), and $N_c = 14.45$M (bottom frame), when $N = 10^5$ and SQ boundary. Points, which yield the maximum life-span, are denoted by arrows in each cases of N_c.

the number of holes which yield $\ell_{\max}$ is unity in all the frames in figure 10. The magnitude of $\mathscr{R}_b$ obtained using $\ell_{\max}$ increases in accordance with the increase in N_c, as shown in the right-half frame of figure 10, because the growth of clusters of granular discs tends to enlarge the vacant space. The PD has the clear structure at $N_c = 0$, whereas such a clear structure in the PD becomes blurred at $N_c = 14.45$M.

The expeditious method to read the characteristics of the PD is to calculate the life-span-distribution (lsd) by each time step. Then, we approximate the lsd, namely, $f(\ell) := (1/N)\sum_{i=1}^{N} \delta(\ell - \ell_i)$ with

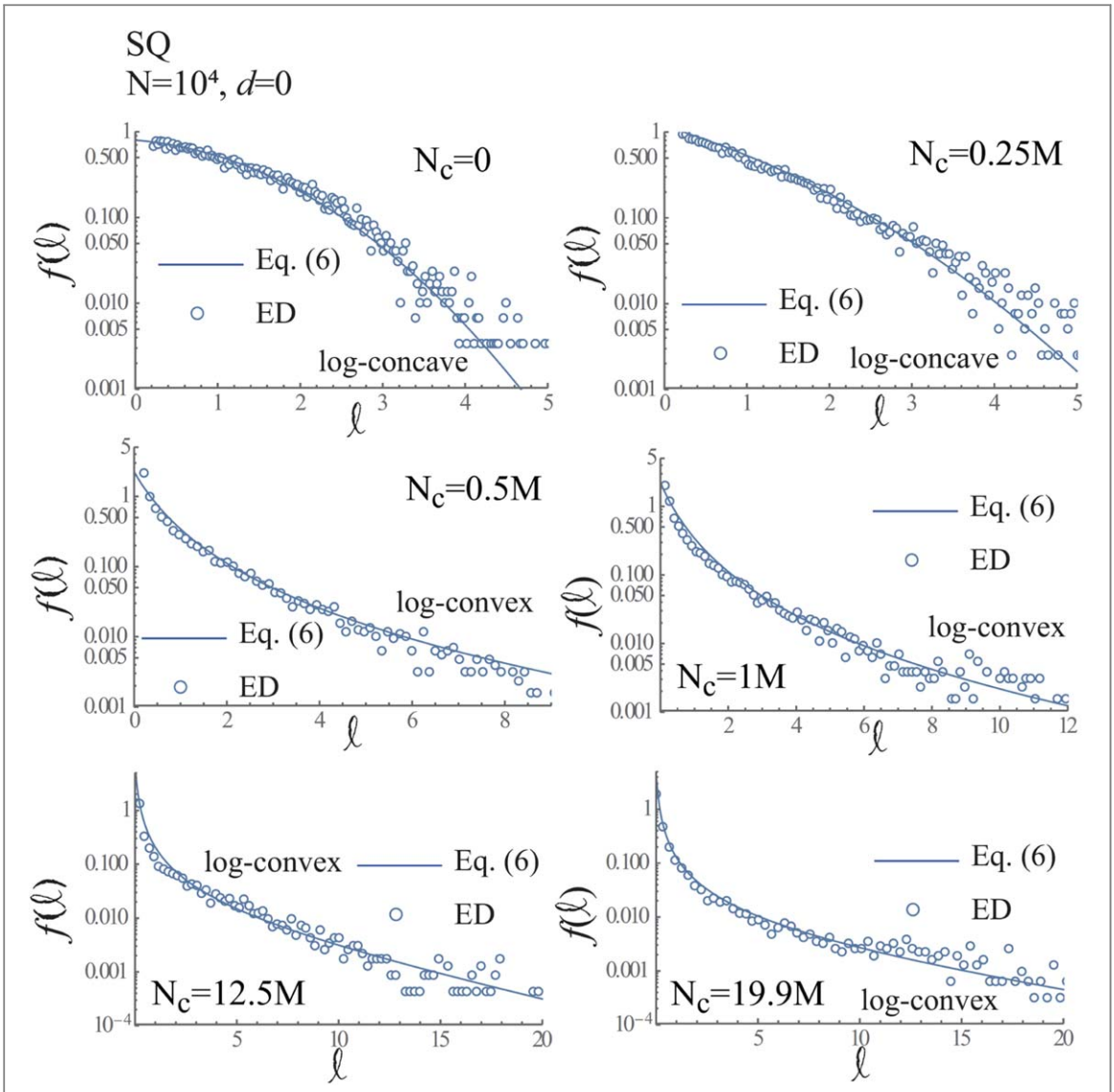

Figure 11. $f(\ell)$ versus ℓ at $N_c = 0$ (top-left frame), $N_c = 0.25$M (top-right frame), $N_c = 0.5$M (middle-left frame), $N_c = 1$M (middle-right frame), $N_c = 12.5$M (middle-left frame), and $N_c = 19.9$M (middle-right frame) obtained using $d = 0$, when $N = 10^4$ and SQ boundary.

$$f_{\rm ap}(\ell) \coloneqq \mathfrak{A}\exp\left[-\mathfrak{B}(\ell - \mathfrak{C})^n\right](\mathfrak{D}\ell + \mathfrak{E})^m \tag{6}$$

where $\mathfrak{A}$, $\mathfrak{B}$, and $\mathfrak{D} \subseteq \mathbb{R}_+$, $\mathfrak{C}$, $\mathfrak{E}$, n and $m \subseteq \mathbb{R}$.

The reason why we use equation (6) is that it can express the hybrid of the logarithmic convex (log-convex: for $\theta \in [0, 1]$, $\theta \log f(x) + (1 - \theta)\log f(y) \leqslant \log f(\theta x + (1 - \theta)y)$ ($a \in \mathbb{R}_+$ and $x < y$)) and logarithmic concave (log-concave: for $\theta \in [0, 1]$, $\theta \log f(x) + (1 - \theta)\log f(y) \geqslant \log f(\theta x + (1 - \theta)y)$ ($a \in \mathbb{R}_+$ and $x < y$)) using appropriate set of (n, m) in equation (6). Similarly, equation (6) is also able to express completely concave or convex for all the range of ℓ (i.e., $\ell \in \mathbb{R}_+$).

Figures 11–16 show $f(\ell)$ versus ℓ together with $f_{\rm ap}(\ell)$ for $d = 0$ (connection) and 1 (hole) in cases of $N = 10^4, 5 \times 10^4$ and 10^5, whose $\mathfrak{A}$, $\mathfrak{B}$, $\mathfrak{C}$, $\mathfrak{D}$, $\mathfrak{E}$, $\mathfrak{F}$, n and m in equation (6) are defined in table 1.

The authors will consider that one standard for the evaluation of the topological phase-transition of the granular discs is determined by the switch between the log-convex and log-concave of $f(\ell)$ (or $f_{\rm ap}(\ell)$), as discussed later. Figure 11 indicates that $f(\ell)$ (or $f_{\rm ap}(\ell)$) follows the log-concave at $N_c = 0$ and 0.25M, whereas $f(\ell)$ (or $f_{\rm ap}(\ell)$) follows the log-convex at 0.5M$\leqslant N_c$. Consequently, we conclude that the topological phase-transition occurs in the range of 0.25M$< N_c <$ 0.5M, when $d = 0$ and $N = 10^4$. Similarly, figure 12 indicates that $f(\ell)$ (or $f_{\rm ap}(\ell)$) follows the log-convex at $\ell \leqslant 9$ and log-concave at $9 < \ell$ in the case of $N_c = 0$, whereas $f(\ell)$ (or $f_{\rm ap}(\ell)$) follows the log-convex at $0 \leqslant \ell$. As a result, the topological phase-transition occurs in the range of $N_c \in$ [0, 1M], when $d = 1$ and $N = 10^4$. These topological phase-transitions are obtained at $N_c \in$ [1M,1.5M] in both cases of $d = 0$ and 1, when $N = 5 \times 10^4$, as shown in figures 13 and 14, whereas it is obtained at $N_c \in$ [2.15M,3.85M] in both cases of $d = 0$ and 1, when $N = 10^5$, as shown in figures 15 and 16.

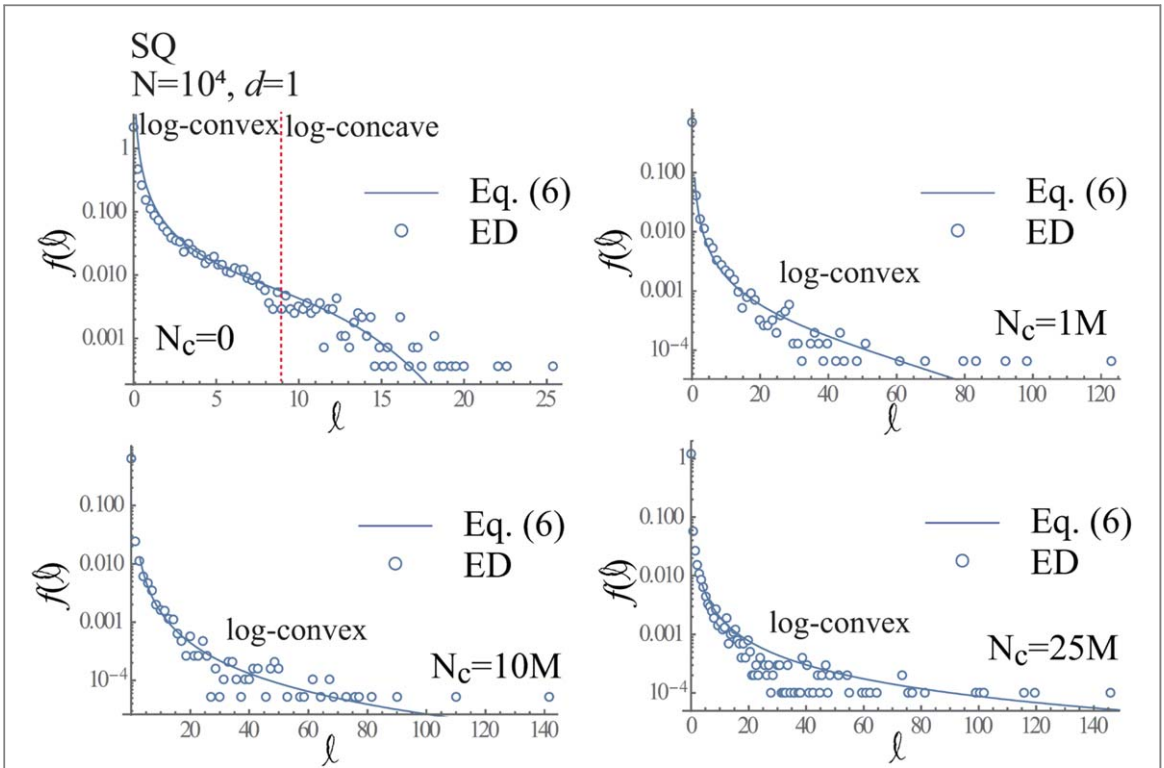

Figure 12. $f(\ell)$ versus ℓ at $N_c = 0$ (upper-left frame), $N_c = 1$M (upper-right frame), $N_c = 10$M (lower-left frame) and $N_c = 25$M (lower-right frame) obtained using $d = 1$, when $N = 10^4$ and SQ boundary.

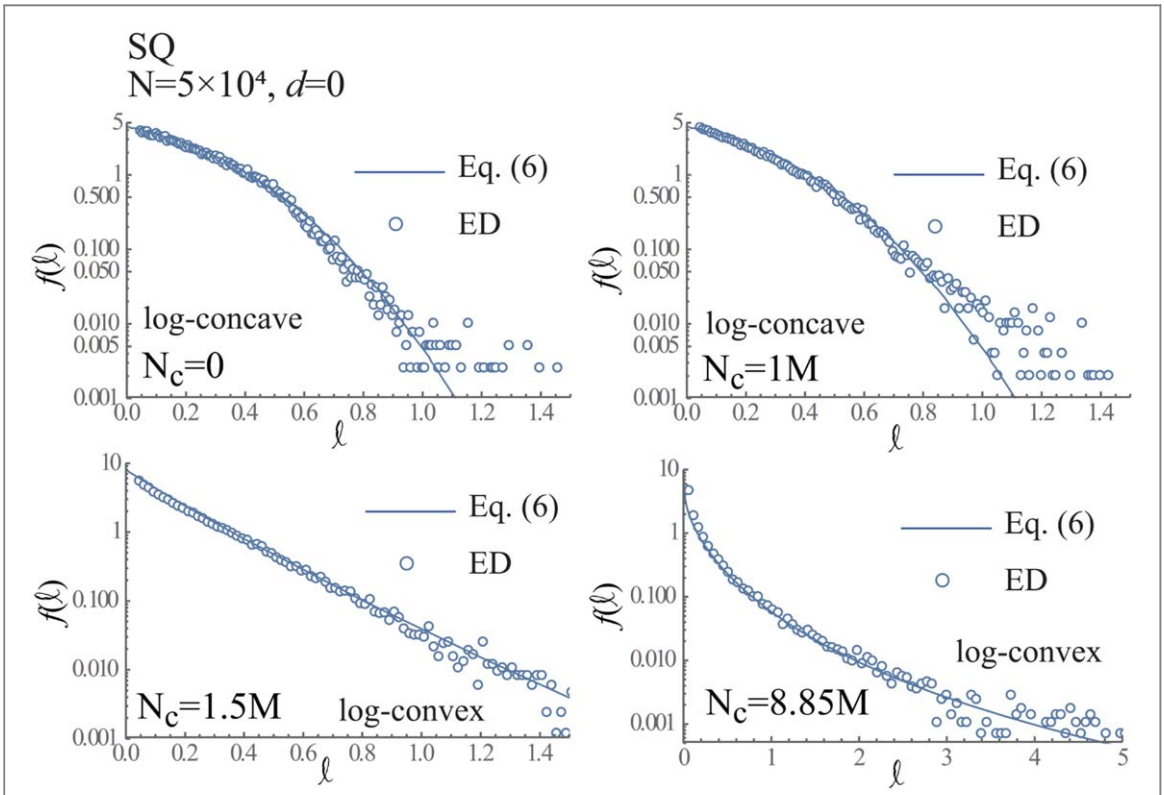

Figure 13. $f(\ell)$ versus ℓ at $N_c = 0$ (upper-left frame), $N_c = 1$M (upper-right frame), $N_c = 1.5$M (lower-left frame) and $N_c = 8.85$M (lower-right frame) obtained using $d = 0$, when $N = 5 \times 10^4$ and SQ boundary.

The lsd obtained using $d = 1$-PD, which follows the log-convex, indicates that the number of holes with the large diameter $\mathscr{R}_d$ and small $\mathscr{R}_b$ (i.e., long life-span) is larger than that obtained using the $d = 1$-PD, which follows the log-concave. The holes with the long life-span are generated by the increase of vacant space and

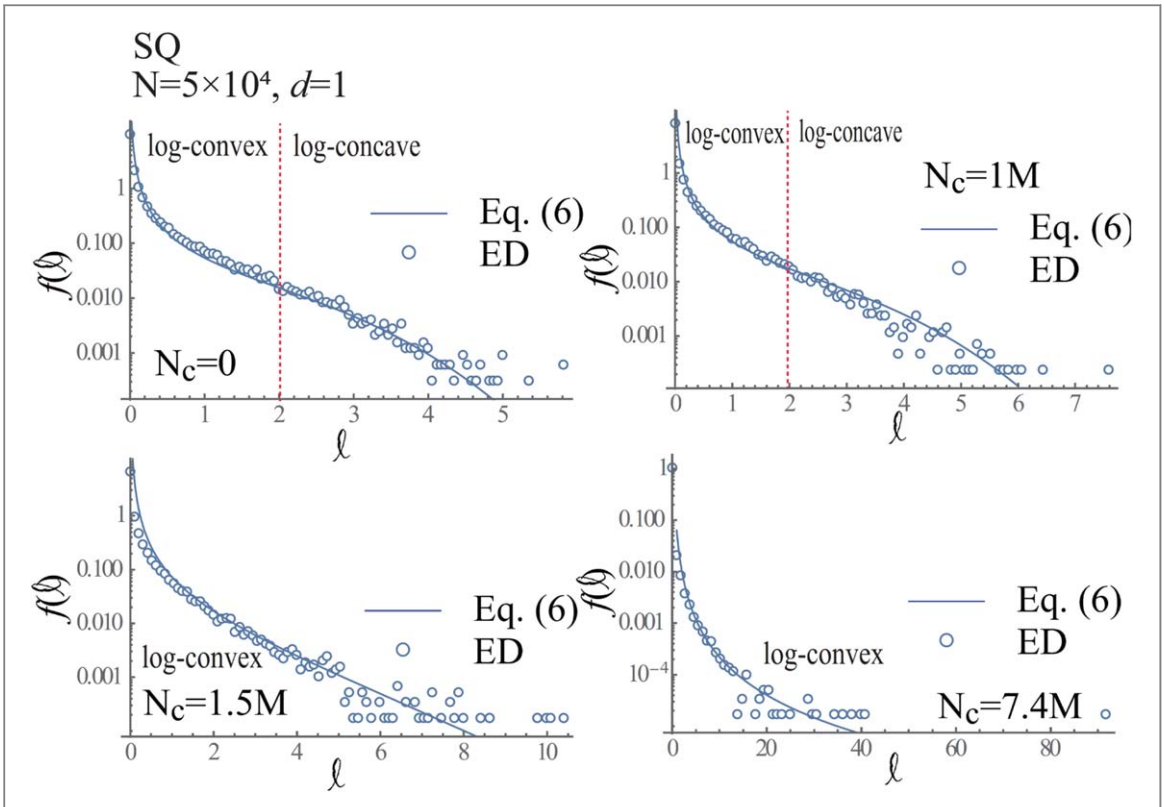

Figure 14. $f(\ell)$ versus ℓ at $N_c = 0$ (upper-left frame), $N_c = 1$M (upper-right frame), $N_c = 1.5$M (lower-left frame), and $N_c = 7.4$M (lower-right frame) obtained using $d = 1$, when $N = 5 \times 10^5$ and SQ boundary.

connections of point-clouds by small $\mathscr{R}_b$, which are caused by the growths of clusters. Consequently, the switch between the log-concave and log-convex becomes the standard to measure the drastic growth of clusters, by which the topological characteristics of granular gases changes, markedly.

From above discussions, we confirmed that the topological phase-transition can be judged by the switch of the life-span-distribution (lsd) (i.e., $f(\ell)$) between the log-convex and log-concave. Here, we investigate the topological phase-transition using the Betti number, B_0 (the zeroth order) and B_1 (the first order). As discussed in section 2, the Betti number is calculated using the PNG versions of figures 7–9. Therefore, the accuracies of the calculations of B_0 and B_1 depend on the number of pixels in PNG versions of figures 7–9. Figure 17 shows B_0/N and B_1/N in cases of $N = 10^4$ (upper-left frame), 5×10^4 (upper-right frame) and $N = 10^5$ (lower-left frame). $B_0/N \simeq 0.96$ at $N_c = 0$ obtained using $N = 10^5$ indicates that the numerical error exists owing to the insufficient number of pixels, whereas $B_0/N = 1$ at $N_c = 0$ obtained using $N = 10^4$ and 5×10^4 indicate that the number of pixels is adequate to calculate B_0 and B_1 with the good accuracy.

Firstly, we confirm that there exist typical three phases (i.e., phases-I, II and III) in cases of $N = 5 \times 10^4$ and 10^5. In the phase-I, B_0 (B_1) decreases (increases), drastically, as shown in $N_c \in [0,0.5\text{M}]$ when $N = 5 \times 10^4$, and $N_c \in [0,1\text{M}]$ when $N = 10^5$. In the phase-II, B_0 (B_1) changes, slightly, as shown in $N_c \in [0.5\text{M},1.5\text{M}]$ when $N = 5 \times 10^4$ and $N_c \in [1\text{M},2\text{M}]$ when $N = 10^5$. Finally, in the phase-III, B_0 (B_1) decreases (increases), drastically, as shown in $N_c \in [1.5\text{M}, \infty)$ when $N = 5 \times 10^4$ and $N_c \in [2\text{M}, \infty)$ when $N = 10^5$. We are, however, unable to identify phases-I and II, clearly, when $N = 10^4$, whereas the phase-III is conformed in $N_c \in [0.25\text{M}, \infty)$, when $N = 10^4$. The increase and decrease in B_0 and B_1 in the phase-III are caused by temporal changes in form of rotating cluster along the wall obtained using $N = 10^4$, so that such changes in phase-III do not attribute to intrinsic changes in the topological phase, which characterize the pattern formation from the HCS. It is the significant result that the topological phase-transition from the phase-I to the phase-II is identified by not the lsd but B_0 and B_1, whereas the phase-transition due to the topological phase-transition from the phase-II to the phase-III is identified by both the lsd and B_0 and B_1.

3.2. Results in case of CI boundary

Now, we investigate the PH in the case of the CI boundary in order to investigate the effects of form of the elastic wall on the PH. The radius of the granular disc (r_d) is set as $r_d = 0.15$ and radius of the CI (R_d) is set as $R_d = 150$. The set of the restitution coefficient and initial velocities of the granular discs are same as those used in calculations in the case of the SQ boundary. The total number of the granular discs (N) is set as $N = 10^5$. As a

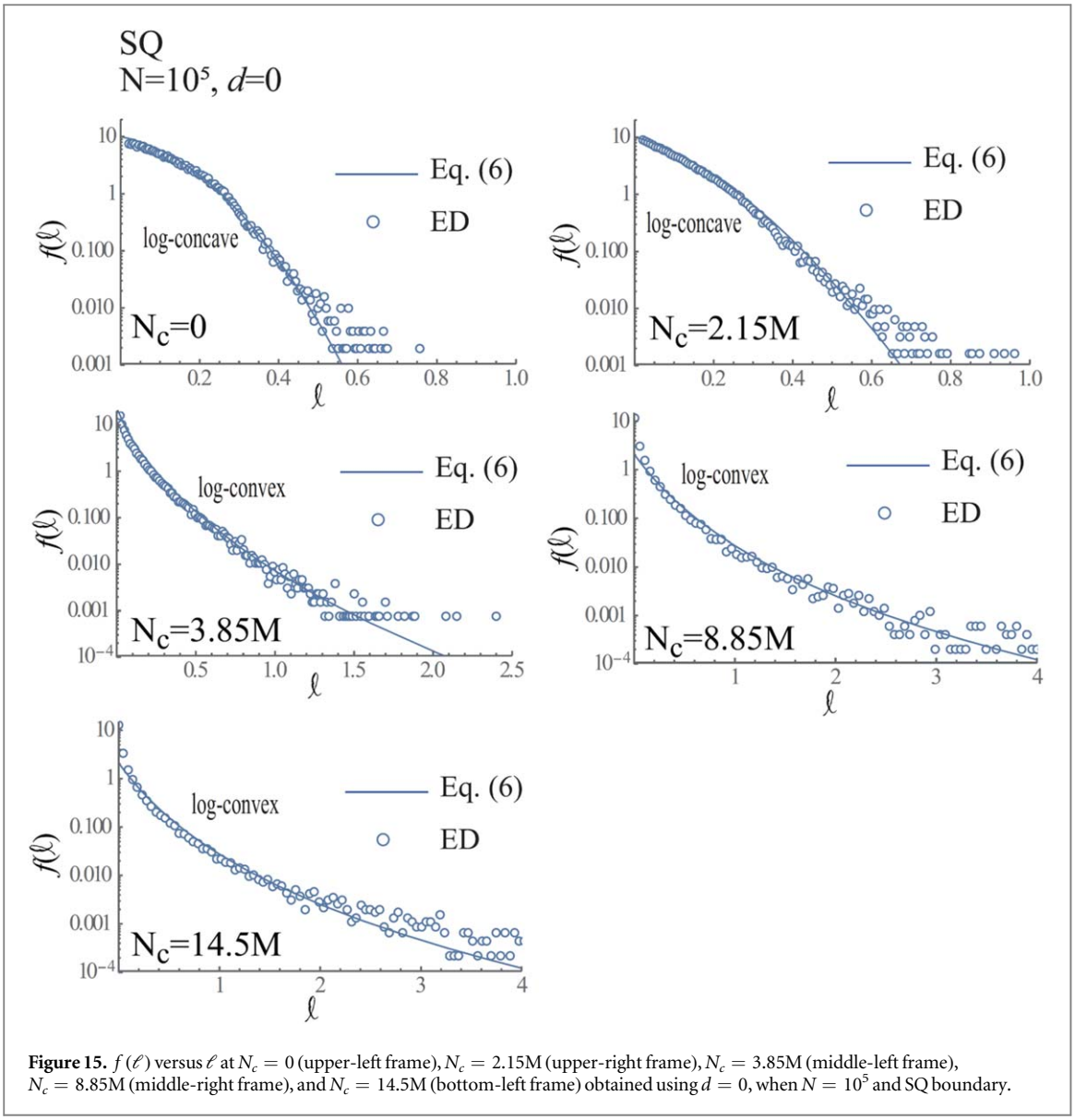

Figure 15. $f(\ell)$ versus ℓ at $N_c = 0$ (upper-left frame), $N_c = 2.15$M (upper-right frame), $N_c = 3.85$M (middle-left frame), $N_c = 8.85$M (middle-right frame), and $N_c = 14.5$M (bottom-left frame) obtained using $d = 0$, when $N = 10^5$ and SQ boundary.

result, the volume fraction of granular discs (ϕ) is calculated as $\phi = 0.1$, because all the granular discs are randomly distributed inside the CI boundary at $t = 0$.

Figure 18 shows snap-shots of the granular discs confined by the CI boundary at $N_c = 0$ (upper-left frame), $N_c = 2.5M$ (upper-center frame), $N_c = 5M$ (upper-right frame), $N_c = 7.5M$ (lower-left frame), $N_c = 15M$ (lower-center frame) and $N_c = 35M$ (lower-right frame). We can confirm the clear pattern formation at $5\text{M} \leqslant N_c$. In particular, the clusters seem to grow from the wall at $N_c = 35$M.

Figure 19 shows the $d = 1$-PDs at $N_c = 0$ (top-left frame), $N_c = 2.5M$ (top-right frame), $N_c = 5M$ (middle-left frame), $N_c = 7.5M$ (middle-right frame), $N_c = 15M$ (bottom-left frame) and $N_c = 35M$ (bottom-right frame), when $N_c = 10^5$ and CI boundary. The tendency of changes in the $d = 1$-PD during the time-evolution is similar to that obtained using the SQ boundary in figure 10. Figures 20 and 21 show $f(\ell)$ versus ℓ together with $f_{\text{ap}}(\ell)$ (in equation (6)) versus ℓ when $d = 0$ and $d = 1$, respectively, where $\mathfrak{A}$, $\mathfrak{B}$, $\mathfrak{C}$, $\mathfrak{D}$, $\mathfrak{E}$, $\mathfrak{F}$, n and m in equation (6) are defined in table 2. We can confirm that the topological phase-transition occurs in $N_c \in$ [2.5M,5M] in both cases of $d = 0$ and 1, as shown in figures 20 and 21.

Figure 22 shows B_0/N, B_1/N and $(B_0 + B_1)/N$. Similarly to B_0/N obtained using $N = 10^5$ and the SQ boundary, $B_0/N \simeq 0.96$ indicates that the numerical error exists owing to the insufficient number of pixels. We can readily confirm that phases-II and III exist in $N_c \in$ [0,2M] and $N_c \in$ [2M, ∞). It is not obvious in the present study whether the lack of the phase-I in the case of the CI boundary is caused by the different form of boundary from the SQ boundary or larger volume fraction ($\phi = 0.1$) in CI boundary than that ($\phi = 0.078\,5$) in the SQ boundary. The phase-transition due to the topological phase-transition from the phase-II to the phase-III is obtained using both the lsd and Betti number in the case of the CI boundary.

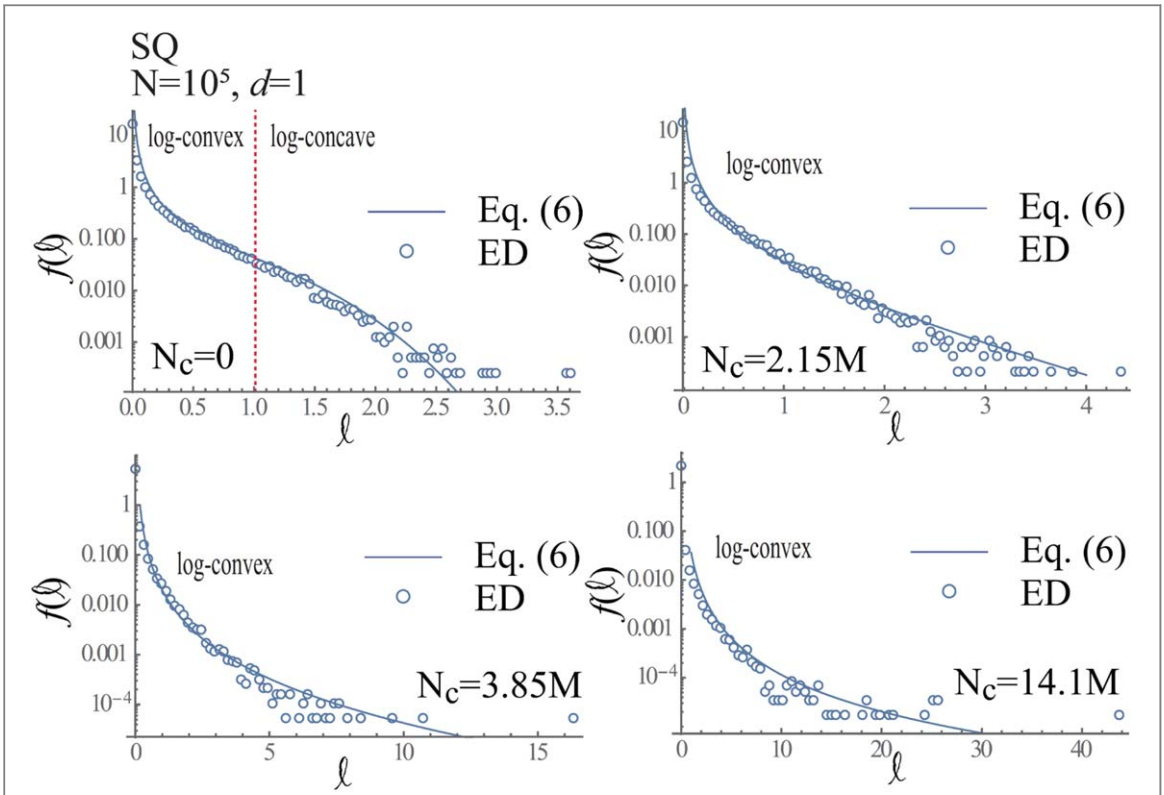

Figure 16. $f(\ell)$ versus ℓ at $N_c = 0$ (upper-left frame), $N_c = 2.15$M (upper-right frame), $N_c = 3.85$M (lower-left frame) and $N_c = 14.1$M (lower-right frame) obtained using $d = 1$ when $N = 10^5$.

3.3. Results in case of SP boundary

Next, we investigate the PH in the case of the SP boundary. As discussed in section 2, the 3D physical space postulates the PH with $d = 2$, which corresponds to the spherical surface (void). Here, we consider two types of N. In one case, $N = 5 \times 10^4$ granular spheres with $r_d = 1.5$ are calculated. In the other case, $N = 10^4$ granular spheres with $r_d = 1.5$ are calculated. In both cases, the radius of the SP boundary is set as $R_d = 150$ and restitution coefficient is set as 0.85. Consequently, the volume fraction is 5% in the case of $N = 5 \times 10^4$ and 1% in the case of $N = 10^4$, because all the granular spheres are randomly (almost homogeneously) distributed inside the SP boundary. The restitution coefficient of the granular spheres is set as 0.85 and the initial velocities of granular spheres are randomly selected in the ranges of $v_x \in [-1, 1]$, $v_y \in [-1, 1]$ and $v_z \in [-1, 1]$.

Figure 23 shows the snapshots of the granular spheres confined by the SP boundary, when $N = 10^4$ (upper two raw) and $N = 5 \times 10^4$ (lower two raw). The granular spheres cluster in the vicinity of the SP boundary with the band-like form as N_c increases, when $N = 10^4$,. On the other hand, some band-like distributions of granular spheres emerge along the SP boundary in accordance with the increase in N_c when $N = 5 \times 10^4$. The aggregation of granular spheres in the vicinity of the wall at large N_c is similar to those in 2D cases of the SQ and CI boundaries.

Figures 24–27 show time-evolutions of $d = 1$-PDs and $d = 2$-PDs obtained using $N_c = 10^4$ and 5×10^4, respectively. The tendency of temporal changes in $d = 1$-PDs is similar to those obtained using the SQ and CI boundaries. $d = 2$-PDs obtained using $N = 10^4$ indicate that the life-spans of most of granular spheres approach to zero at $N_c = 5.5$M, when $N = 10^4$, although the life-spans of some of granular spheres are finite, as observed in $d = 1$-PD at $N_c = 5.5$M in figure 24. Meanwhile, the life-spans of granular spheres observed in $d = 2$-PDs are finite at $N_c = 40$M, when $N = 5 \times 10^4$, as shown in figure 27.

Figures 28–33 show $f(\ell)$ versus ℓ together with $f_{\rm ap}(\ell)$ versus ℓ obtained using $N = 10^4$ and 5×10^4, when $d = 0$, 1 and 2, respectively, where $\mathfrak{A}$, $\mathfrak{B}$, $\mathfrak{C}$, $\mathfrak{D}$, $\mathfrak{E}$, $\mathfrak{F}$, n and m in equation (6) are defined in table 3. Figures 28 and 30 indicate that the topological phase-transition occurs in $N_c \in$ [2M,2.5M] in the case of $N = 10^4$, whereas all of $f(\ell)$ for $d = 2$ follow log-convex at $N_c \in [0, \infty)$, when $N = 10^4$, as shown in figure 32. Similarly, the topological phase-transition occurs in $N_c \in$[3M,4M], when $N = 5 \times 10^4$, as shown in figure 29. The log-concave of $f(\ell)$ remains at $N_c = 45$M, when $d = 1$ and $N = 5 \times 10^4$, as shown in figure 31. Then, we cannot determine the topological phase-transition from the lsd for $d = 1$, when $N = 5 \times 10^4$. Similarly to $f(\ell)$ obtained using $d = 2$ and $N = 10^4$, all of $f(\ell)$ follow the log-convex in $N_c \in [0, \infty)$, as shown in figure 33. Consequently, we conclude that the lsd for $d = 2$ can not be used as the standard, which determines the

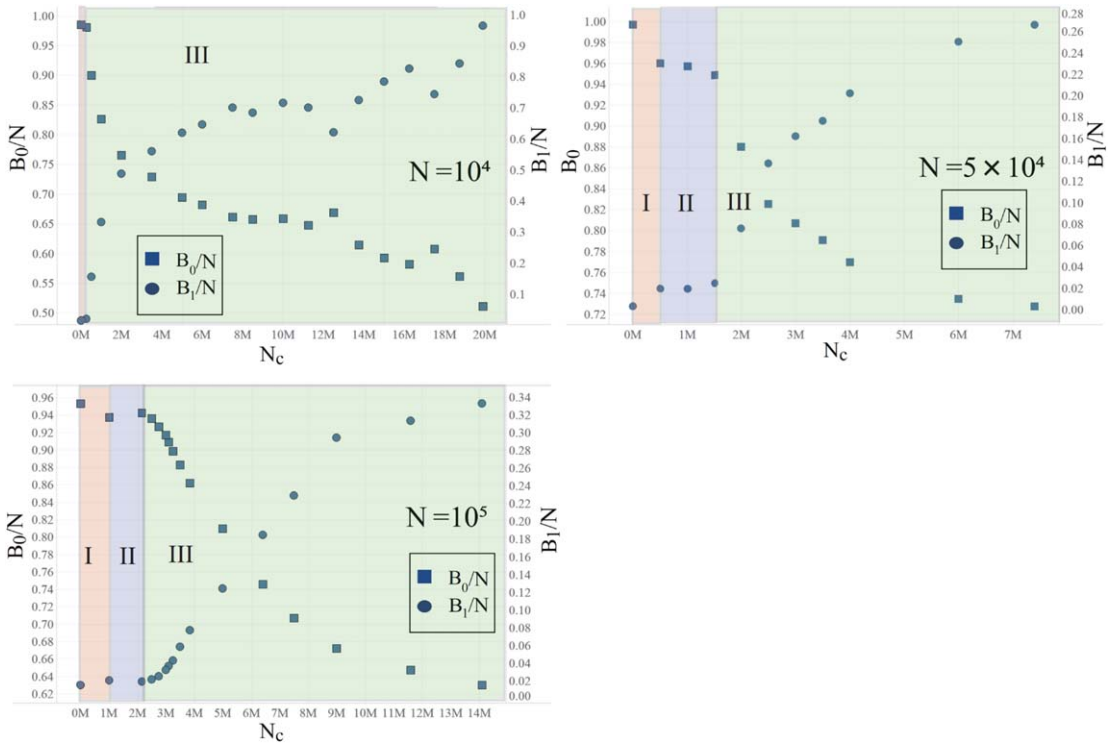

Figure 17. B_0 and B_1 versus N_c, when $N = 10^4$ (upper-left frame), 5×10^4 (upper-right frame) and 10^5 (lower-left frame).

Table 1. $\mathfrak{A}$, $\mathfrak{B}$, $\mathfrak{C}$, $\mathfrak{D}$, $\mathfrak{E}$, n and m in equation (6) and corresponding figure number, when $d = 0$ and 1, $N = 10^4$, 5×10^4 and 10^5, and SQ boundary are used.

Form	d	N	N_c	$\mathfrak{A}$	$\mathfrak{B}$	$\mathfrak{C}$	$\mathfrak{D}$	$\mathfrak{E}$	n	m	Figure No.
SQ	0	10^4	0	0.8	0.29	0	1	1	2	0.2	Figure 11
SQ	0	10^4	2.5M	1.2	0.29	0	1	1	1.8	0.35	Figure 11
SQ	0	10^4	5M	2.25	0.15	0	1	1	0.8	−2.5	Figure 11
SQ	0	10^4	12.5M	0.25	0.05	0	1	0.1	1.26	−1.5	Figure 11
SQ	0	10^4	19.9M	0.15	0.03	0	1	1	1.26	−1.5	Figure 11
SQ	0	5×10^4	0	4.5	5.5	0	1	1	2.2	−2	Figure 13
SQ	0	5×10^4	1M	4.5	5.5	0	1	1	2.2	−2	Figure 13
SQ	0	5×10^4	1.5M	8	3.25	0	1	1	1	−3	Figure 13
SQ	0	5×10^4	8.85M	12	3.25	0	1	1	0.25	−3	Figure 13
SQ	0	10^5	0	10	25	0	1	1	2	−3	Figure 15
SQ	0	10^5	2.15M	10	15	0	1	1	1.7	−3	Figure 15
SQ	0	10^5	3.85M	8	4.2	0	1	0.75	0.5	−5	Figure 15
SQ	0	10^5	8.85M	0.5	0.1	0	1	0.75	1.2	−5	Figure 15
SQ	0	10^5	14.5M	0.5	0.1	0	1	0.75	1.2	−5	Figure 15
SQ	1	10^4	0	0.003	2.5×10^{-5}	0	0.067	10^{-5}	4	−1.5	Figure 12
SQ	1	10^4	1M	0.005	6.1×10^{-9}	0	0.2	10^{-5}	2	−1.5	Figure 12
SQ	1	10^4	5M	0.005	2.2×10^{-10}	0	0.2	10^{-5}	3.2	−1.75	Figure 12
SQ	1	10^4	12.5M	0.005	3.57×10^{-22}	0	0.2	10^{-5}	6.2	−1.35	Figure 12
SQ	1	5×10^4	0	5×10^{-3}	3.14×10^{-2}	0	0.2	10^{-5}	3	−1.5	Figure 14
SQ	1	5×10^4	1M	5×10^{-3}	1.6×10^{-2}	0	0.2	10^{-5}	3	−1.5	Figure 14
SQ	1	5×10^4	1.5M	5×10^{-3}	0.136	0	0.2	10^{-5}	1.5	−1.75	Figure 14
SQ	1	5×10^4	7.4M	1.2×10^{-3}	3.79×10^{-3}	0	0.2	10^{-5}	0.98	−2.4	Figure 14
SQ	1	10^5	0	5×10^{-3}	0.25	0	0.5	0	3	−1.5	Figure 16
SQ	1	10^5	2.15M	0.02	1	0	0.4	0	1	−1.5	Figure 16
SQ	1	10^5	3.85M	0.01	0.71	0	0.4	0	0.5	−2	Figure 16
SQ	1	10^5	14.5M	0.01	1	0	0.4	0	1.5×10^{-3}	−2.5	Figure 16

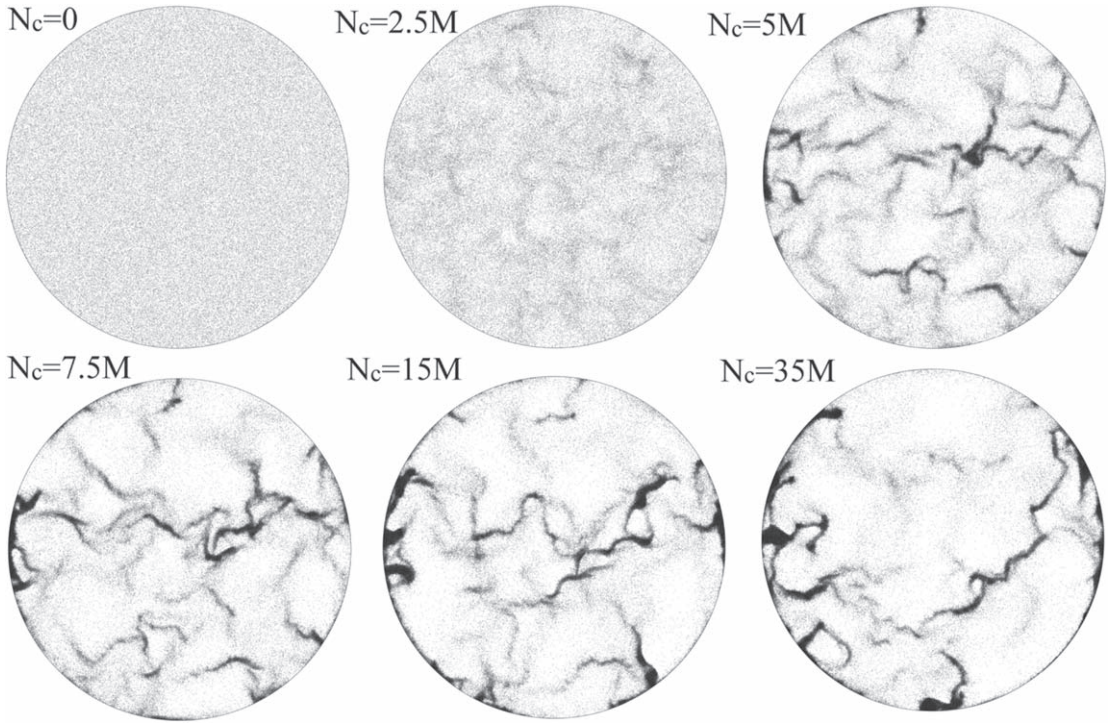

Figure 18. Snap-shots of granular discs confined by CI boundary at $N_c = 0$ (upper-left frame), $N_c = 2.5M$ (upper-center frame), $N_c = 5M$ (upper-right frame), $N_c = 7.5M$ (lower-left frame), $N_c = 15M$ (lower-center frame) and $N_c = 35M$ (lower-right frame).

topological phase-transition in accordance with the switch of the lsd between the log-concave and log-convex in both cases of $N = 10^4$ and 5×10^5.

The Betti number is not calculated in the case of the SP boundary, because the monotone (0,1) pixels, which are used in the calculation of B_0 and B_1 in the SQ and CI boundaries, are unable to consider the depth-direction in 3D.

4. 3D crystal classification of granular gases by VA BAA and PTM

Based on the numerical results obtained using the SP boundary in section 3, we investigate the 3D crystal classification of the granular gases confined by the SP boundary using the Voronoi's analysis (VA), bond-angle analysis (BAA) and polyhedral template matching (PTM). The numerical schemes of the VA, BAA and PTM have been already demonstrated in section 2, briefly. As discussed in Introduction, there are two goals in our study of the granular gases with the VA, BAA and PTM. One is to confirm whether the VA, BAA or PTM are able to identify the transition of the granular gases from the HCS to the clustering state or not. The other is to investigate which typical coordination (i.e., FCC, BCC, HCP, ICO etc.,) the crystal structures of the granular particles, which are condensed around the wall, densely, are categorized using the VA, BAA and PTM. We proceed our discussions of analytical results in order of the BAA, VA and PTM.

4.1. Results of BAA

Figure 34 shows snapshots of the categorized coordination per a granular particle and its fraction obtained using the BAA at $N_c = 0, 4M, 5M, 6M, 10M, 20M, 30M, 40M$ and $47.4M$. We can confirm that the spatially random locations of granular spheres at $N_c = 0$ ($t = 0$) does not obtain any crystal structure. In short, all the coordination of granular particles is categorized as *Other*. Meanwhile, the fraction of granular spheres with the coordination categorized as the HCP, FCC and BCC (coordination) increases, as N_c increases. Actually, 20% of granular spheres are categorized as the structured coordination, namely, FCC, HCP, BCC and ICO at $N_c = 47.7$M. Of course, most of granular spheres condensate around the wall at $N_c = 47.7$M, so that such a status is not appropriate to be called as the *granular gases*.

Figure 35 shows the fractions of the categories of the coordination versus N_c obtained using the BAA (*Other*: left frame, FCC, HCP, BCC and ICO: right frame). The enlarged figure (log-log plot of the fraction of *Other*

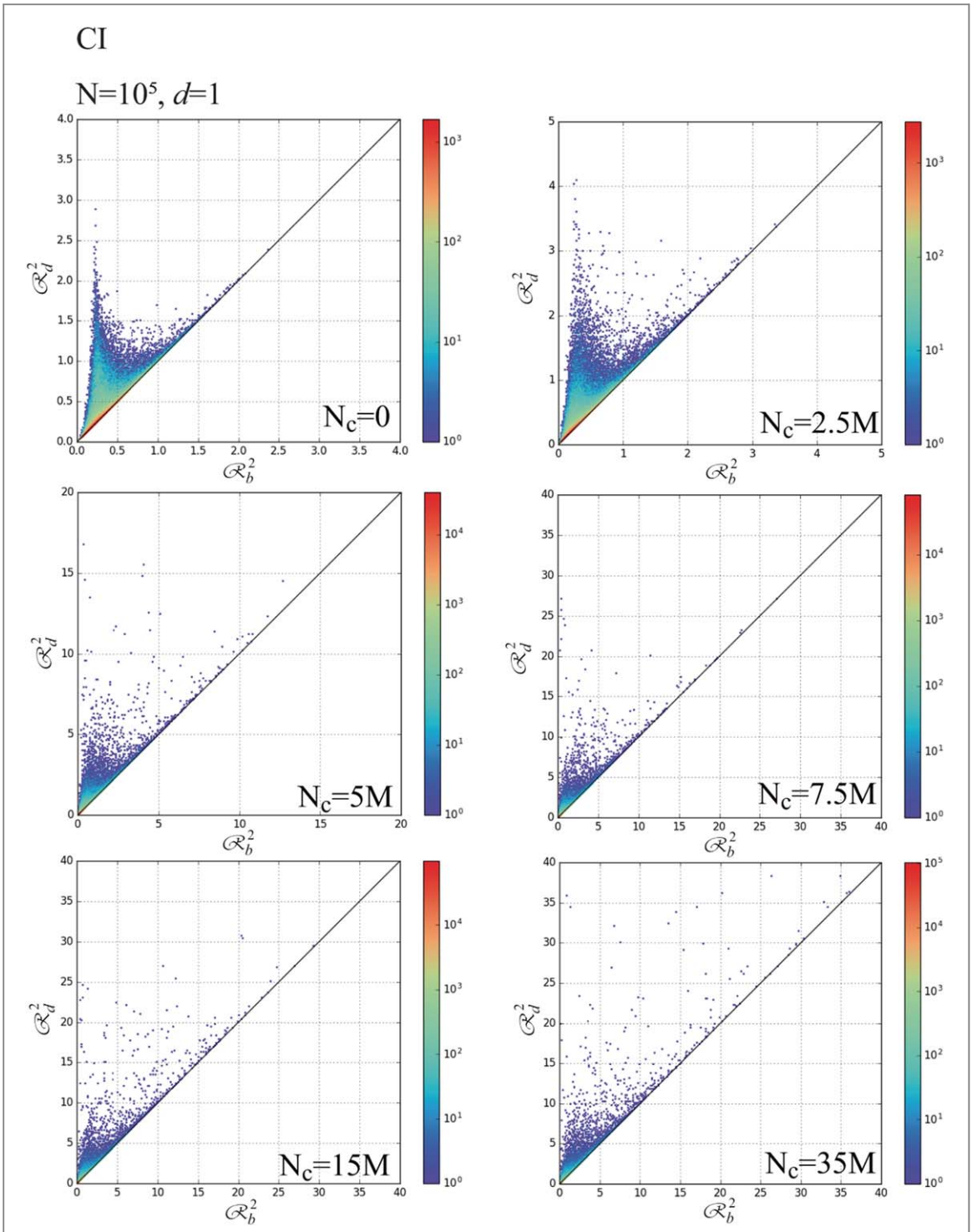

Figure 19. PD obtained using $d = 1$ at $N_c = 0$ (top-left frame), $N_c = 2.5M$ (top-right frame), $N_c = 5M$ (middle-left frame), $N_c = 7.5M$ (middle-right frame), $N_c = 15M$ (bottom-left frame) and $N_c = 35M$ (bottom-right frame), when $N_c = 10^5$ and CI-boundary.

versus N_c) is added to the left frame of figure 35 in order to show that the fraction of *Other* decreases by the inverse power law function of N_c. As shown in figure 35, the fraction of the category of the coordination is invariant during $N_c < 4M$ and decreases in accordance with $130/(N_c/M + 4)^{-0.125}$. Then, we can discriminate the topological phase of the granular spheres between $N_c < 4M$ (HCS) and $4M \leqslant N_c$ (growth of clusters). Reminding that the lsd for $d = 0$ changes from the log-concave to the log-convex at $3M < N_c < 4M$, as shown in figure 29, the BAA also specifies the topological phase-transition of the granular spheres with a similar accuracy to the lsd obtained using $d = 0$-PD.

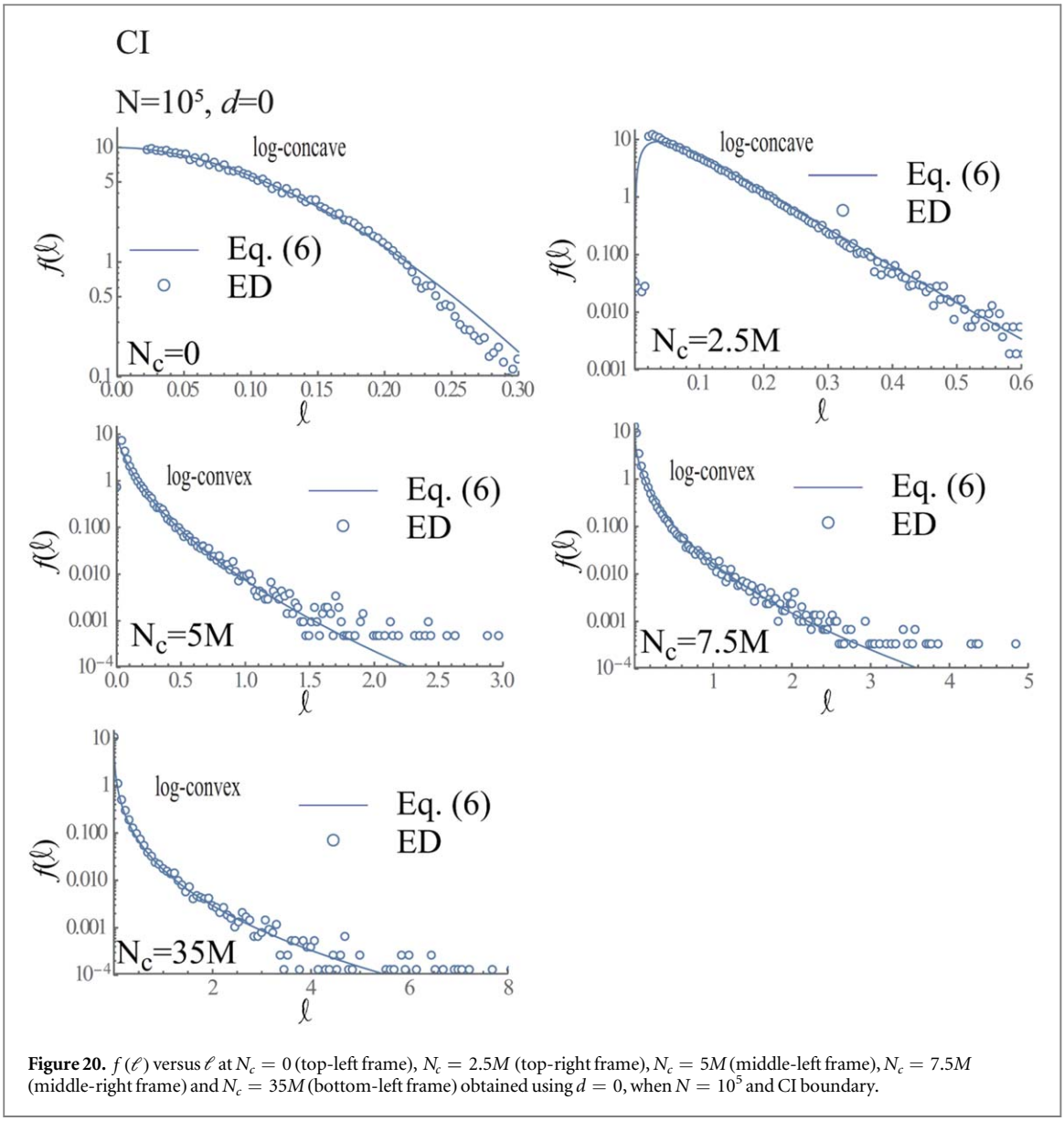

Figure 20. $f(\ell)$ versus ℓ at $N_c = 0$ (top-left frame), $N_c = 2.5M$ (top-right frame), $N_c = 5M$ (middle-left frame), $N_c = 7.5M$ (middle-right frame) and $N_c = 35M$ (bottom-left frame) obtained using $d = 0$, when $N = 10^5$ and CI boundary.

4.2. Results of VA

Figure 36 shows the snapshots of the categorized coordination per a granular sphere and its fraction at $N_c = 0$, 2M 4M, 5M, 6M, 10M, 20M, 30M, 40M and 47.4M obtained using the VA. We can confirm that 3.1% of randomly located granular spheres at $N_c = 0$ can be categorized as HCP or FCC (coordination). Finally, 32.8% of granular spheres obtain the crystal structures, namely, FCC, HCP, BCC, FCC-HCP and ICO at $N_c = 47.7$M.

Figure 37 shows the fractions of the categories of the coordination versus N_c obtained using the VA (*Other*: left frame, FCC, BCC, ICO, FCC-HCP and HCP: right frame). The enlarged figure (log-log plot of the fraction of *Other* versus N_c) is added to the left frame of figure 34 in order to show that the fraction of *Other* decreases by the inverse power law function of N_c. As shown in figure 34, the fraction of the category *Other* is almost invariant during $N_c <$ 4M and decreases in accordance with $145/(N_c/M + 4)^{-0.2}$. Then, the VA-results indicate that the topological phase-transition of the granular spheres occurs between $N_c <$ 4M (HCS) and 4M$\leqslant N_c$ (growth of clusters) similarly to the PD and BAA. The growths of the fractions of the FCC-HCP and HCP are markedly larger than those of the BCC, ICO and FCC. Then, we can conclude that the HCP type coordination is dominant in both cases of the BAA and VA, when the structured coordination are assigned to granular spheres.

4.3. Results of PTM

We consider the categorization of the coordination obtained using the PTM. Figures 38–46 show granular particles inside the SP boundary, which are colored in accordance with the assigned category of the coordination (i.e., All:=*Other*, FCC, HCP, BCC, ICO and SC), at $N_c = 0$, 4M, 5M, 6M, 10M, 20M, 30M, 40M, and 47.7M together with $\sum_{XX} f_{XX}(\ell_{\mathrm{RMSD}})$ versus ℓ_{RMSD} (XX:=FCC, HCP, BCC, ICO and SC) in their top-left frames.

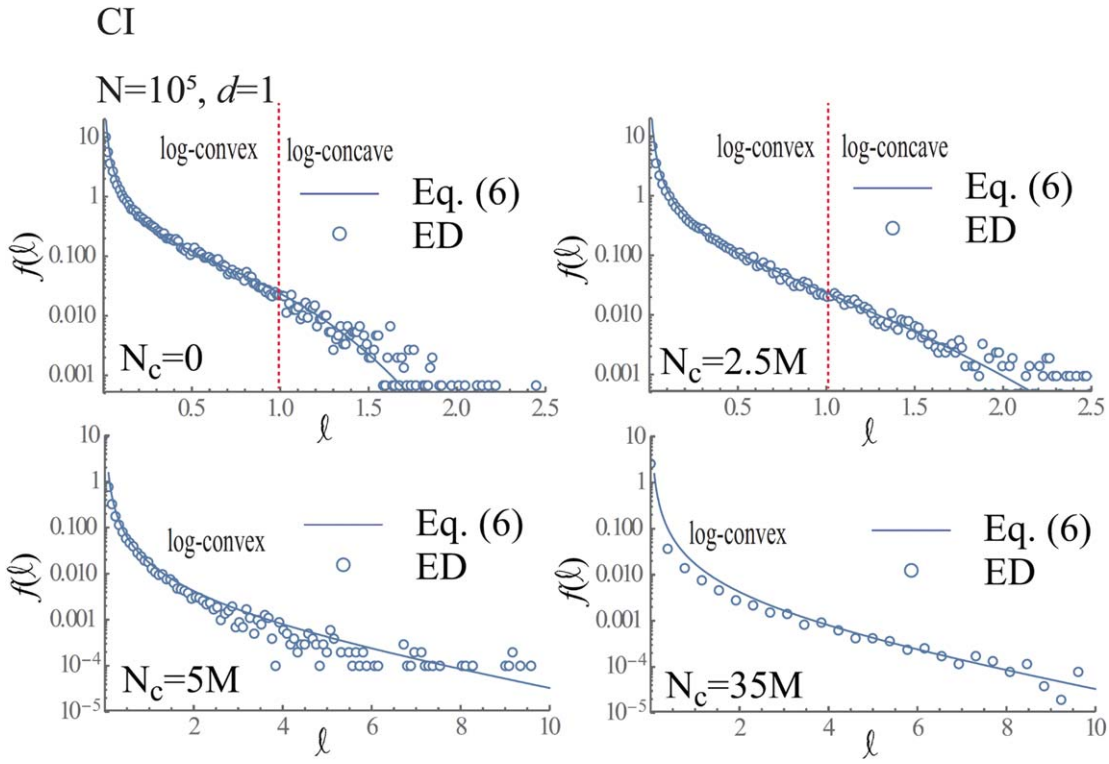

Figure 21. $f(\ell)$ versus ℓ at $N_c = 0$ (upper-left frame), $N_c = 2.5M$ (upper-right frame), $N_c = 5M$ (lower-left frame), and $N_c = 35M$ (lower-right frame) obtained using $d = 1$, when $N = 10^5$ and CI boundary.

Table 2. $\mathfrak{A}$, $\mathfrak{B}$, $\mathfrak{C}$, $\mathfrak{D}$, $\mathfrak{E}$, n and m in equation (6) and corresponding figure number, when $d = 0$ and 1, $N = 10^5$ and CI boundary are used.

Form	d	N	N_c	$\mathfrak{A}$	$\mathfrak{B}$	$\mathfrak{C}$	$\mathfrak{D}$	$\mathfrak{E}$	n	m	figure No.
CI	0	10^5	0	1	34.8	0	1	3.15	1.74	2	Figure 20
CI	0	10^5	2.5M	900	18	0	1	-10^{-4}	0.8	1	Figure 20
CI	0	10^5	5M	100	9.5	0	1	-10^{-4}	0.48	0.35	Figure 20
CI	0	10^5	7.5M	50	8	0	1	-10^{-4}	0.4	0.2	Figure 20
CI	0	10^5	35M	50	8	0	1	-10^{-4}	0.3	0.15	Figure 20
CI	1	10^5	0	0.05	0.75	0	1	10^{-7}	3	−1.4	Figure 21
CI	1	10^5	2.5M	0.05	0.75	0	1	10^{-7}	2	−1.4	Figure 21
CI	1	10^5	5M	0.02	0.15	0	1	10^{-7}	1.2	−1.75	Figure 21
CI	1	10^5	35M	0.02	0.15	0	1	10^{-7}	1.2	−1.75	Figure 21

Additionally, other remained frames except for top-left frame in figures 38–46 show the granular particles inside the SP boundary, which are colored by only two categories *Other* and *XX* (*XX*:=FCC, HCP, BCC, ICO and SC) together with the distribution of the RMSD, namely, $f_{XX}(\ell_{\mathrm{RMSD}})$ versus ℓ_{RMSD}, when all the granular particles are categorized by *Other* and *XX* (i.e., FCC, HCP, BCC, ICO and SC). Figure 38 shows that 48.7% of N is categorized as *Other*, whereas 45.3% of N is categorized as the SC and 4.9% of N is categorized as the HCP, at $N_c = 0$. Then, 50.2% of N is categorized as the structured coordination at $N_c = 0$, even when the BAA and VA categorize most of N as *Other*. $f_{\mathrm{All}}(\ell_{\mathrm{RMSD}})$ and $f_{\mathrm{SC}}(\ell_{\mathrm{RMSD}})$ seem to follow Gaussian distributions at $N_c = 0$, respectively. The deviations of $f_{\mathrm{All}}(\ell_{\mathrm{RMSD}})$ from the Gaussian become marked, as N_c increases. For example, $f_{\mathrm{All}}(\ell_{\mathrm{RMSD}})$ has fat tailed distribution at $N_c = 10\mathrm{M}$ and has markedly asymmetric form, when $30\mathrm{M} \leqslant N_c$. In particular, the fat tailed regime of $f_{\mathrm{All}}(\ell_{\mathrm{RMSD}})$ at $\ell_{\mathrm{RMSD}} \leqslant 0.3$ is caused by the plateau distribution of $f_{\mathrm{FCC}}(\ell_{\mathrm{RMSD}})$ at $\ell_{\mathrm{RMSD}} \leqslant 0.3$ and bimodal distribution of $f_{\mathrm{BCC}}(\ell_{\mathrm{RMSD}})$ at $\ell_{\mathrm{RMSD}} \leqslant 0.3$, as shown in figures 44, 45 and 46. Similarly, asymmetry of $f_{\mathrm{SC}}(\ell_{\mathrm{RMSD}})$ becomes marked, when $10\mathrm{M} \leqslant N_c$. Other significant result obtained using the PTM is time-evolutions of $f_{\mathrm{HCP}}(\ell_{\mathrm{RMSD}})$. $f_{\mathrm{HCP}}(\ell_{\mathrm{RMSD}})$ approaches $\exp(-a|\ell_{\mathrm{RMSD}} - 0.27|)$ $(a \in \mathbb{R}_+)$, as N_c increases. Therefore, most of granular particles, which are categorized as the HCP, deviates from the HCP template with the constant distance 0.27 and such $f_{\mathrm{HCP}}(\ell_{\mathrm{RMSD}})$ decreases exponentially, as ℓ_{RMSD} deviates from 0.27.

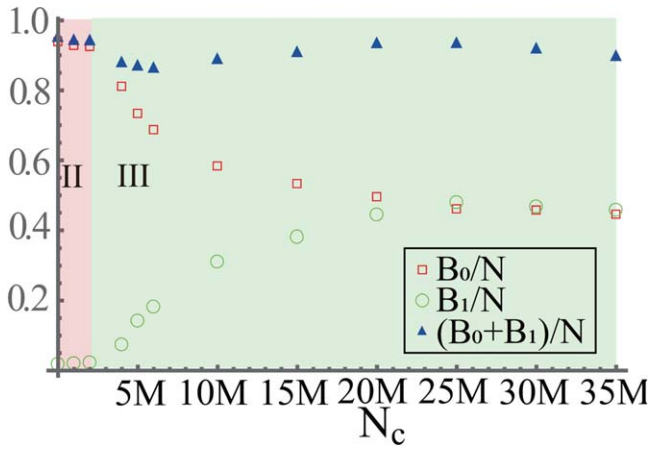

Figure 22. $B_0/N, B_1/N$ and $(B_0 + B_1)/N$ versus N_c obtained using CI boundary.

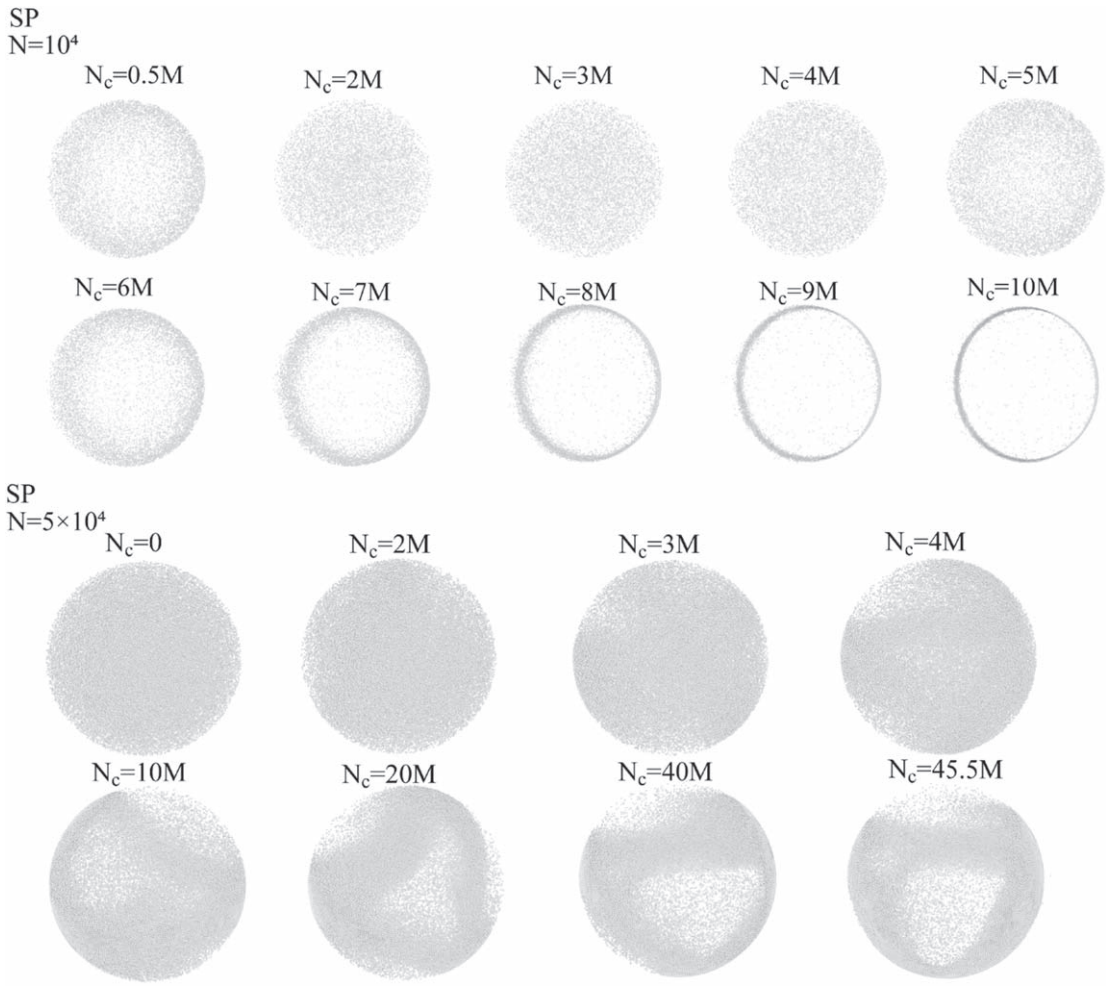

Figure 23. Snapshots of granular spheres confined by SP boundary at each N_c when $N = 10^4$ (upper two raw) and 5×10^4 (lower two raw).

Finally, the left-top frame of figure 47 shows time-evolution of the fraction of categories *XX* (:=*Other*, FCC, HCP, BCC, ICO and SC). The fraction of the HCP increases and becomes comparable with that of the SC, as N_c increases. The temporal change in the fraction of *Other* is not marked in comparison of that obtained using the BAA and VA. The bottom-left and bottom-right frames show good fits of fractions of categories *Other* and SC

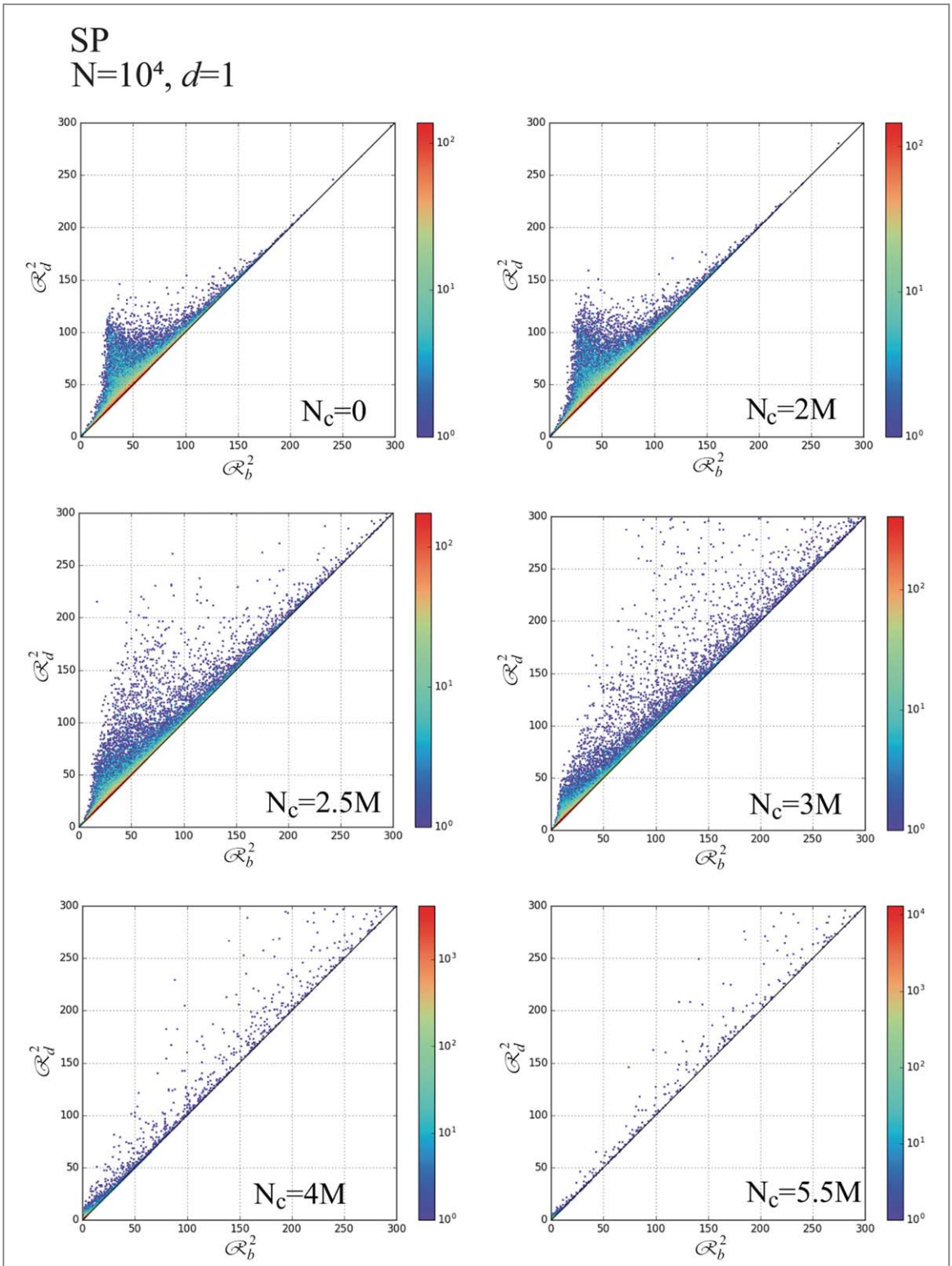

Figure 24. PD obtained using $d = 1$ at $N_c = 0$ (top-left frame), $N_c = 2M$ (top-right frame), $N_c = 2.5M$ (middle-left frame), $N_c = 3M$ (middle-right frame), $N_c = 4M$ (bottom-left frame) and $N_c = 5.5M$ (bottom-right frame), when $N_c = 10^4$ and SP-boundary.

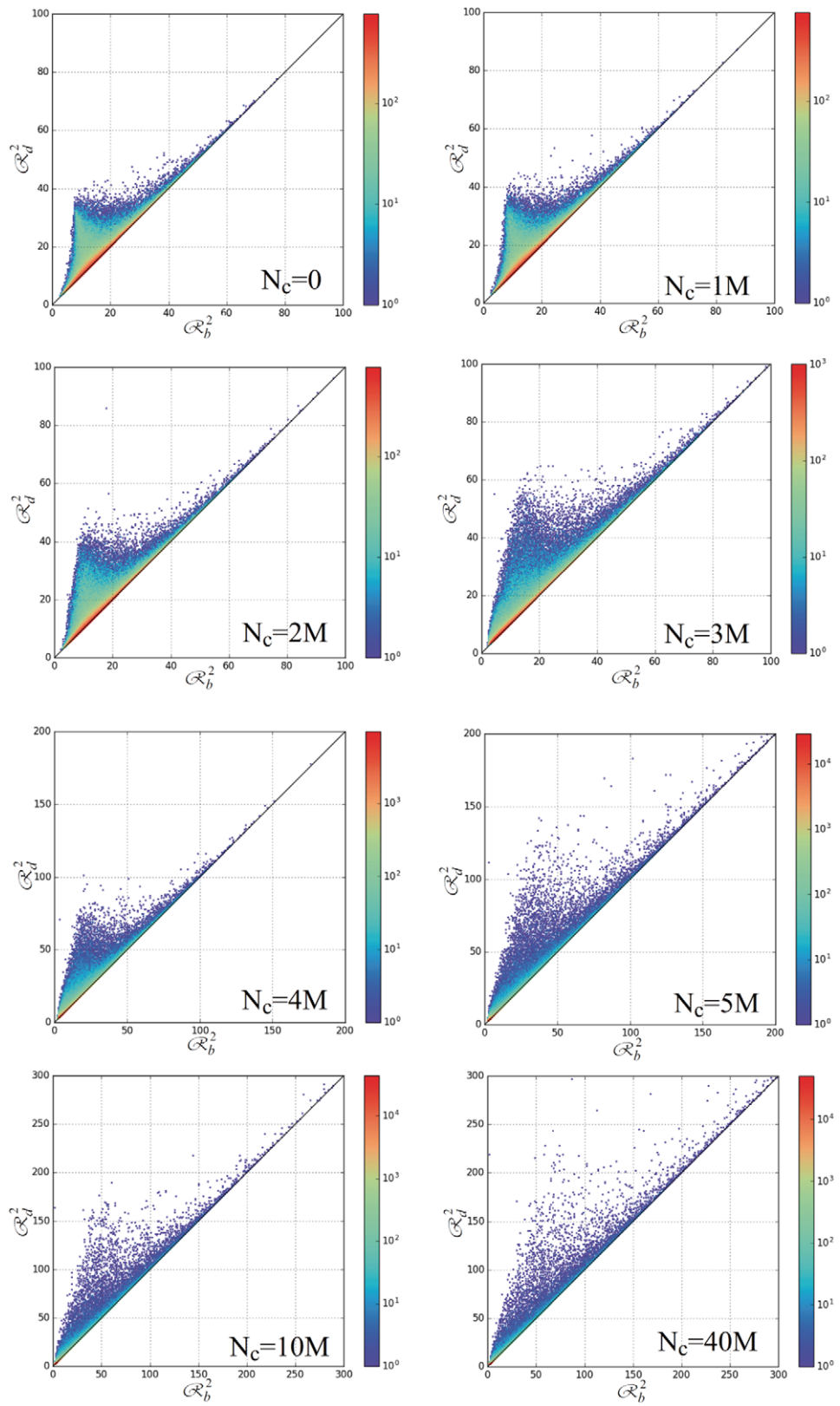

Figure 25. PD obtained using $d = 1$ at $N_c = 0$ (top-left frame), $N_c = 1.5M$ (top-right frame), $N_c = 2M$ (second top-left frame), $N_c = 3M$ (second-right frame), $N_c = 4M$ (second bottom-left frame), $N_c = 5M$ (second bottom-right frame), $N_c = 10M$ (bottom-left frame), $N_c = 40M$ (bottom-right frame), when $N_c = 5 \times 10^4$ and SP-boundary.

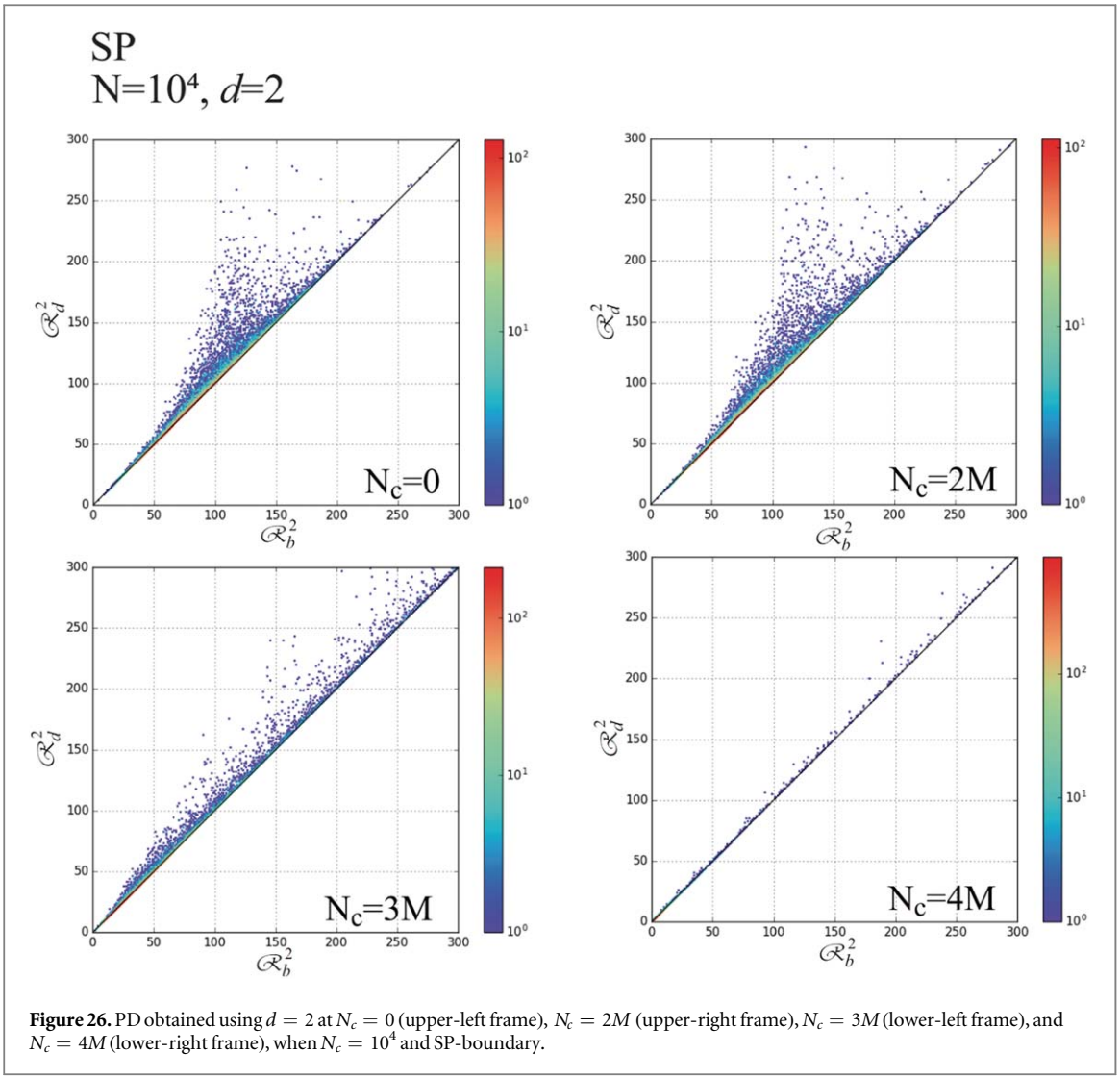

Figure 26. PD obtained using $d = 2$ at $N_c = 0$ (upper-left frame), $N_c = 2M$ (upper-right frame), $N_c = 3M$ (lower-left frame), and $N_c = 4M$ (lower-right frame), when $N_c = 10^4$ and SP-boundary.

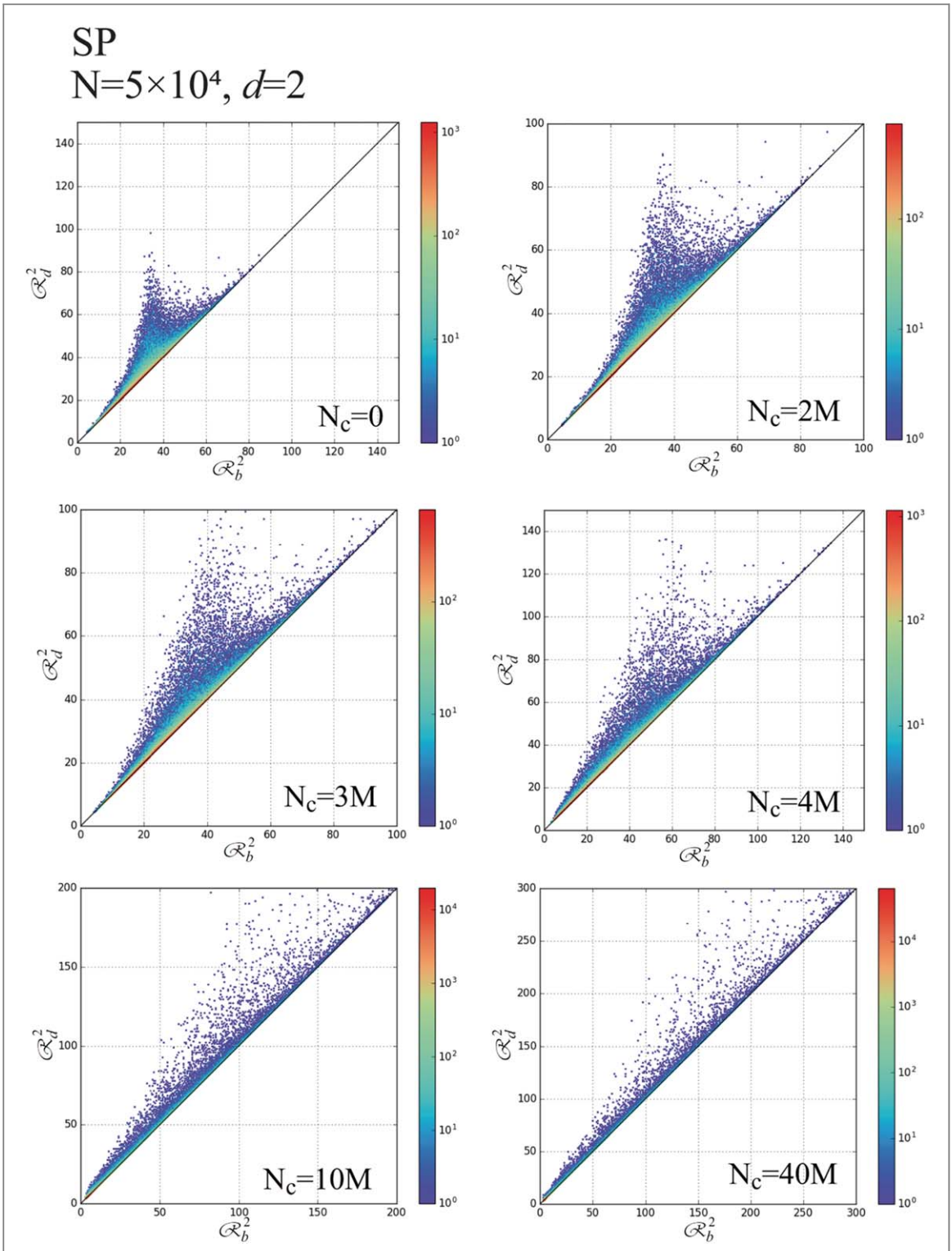

Figure 27. PD obtained using $d = 2$ at $N_c = 0$ (top-left frame), $N_c = 2M$ (top-right frame), $N_c = 3M$ (middle-left frame), $N_c = 4M$ (middle-right frame), $N_c = 10M$ (bottom-left frame), $N_c = 40M$ (bottom-right frame), when $N_c = 5 \times 10^4$ and SP-boundary.

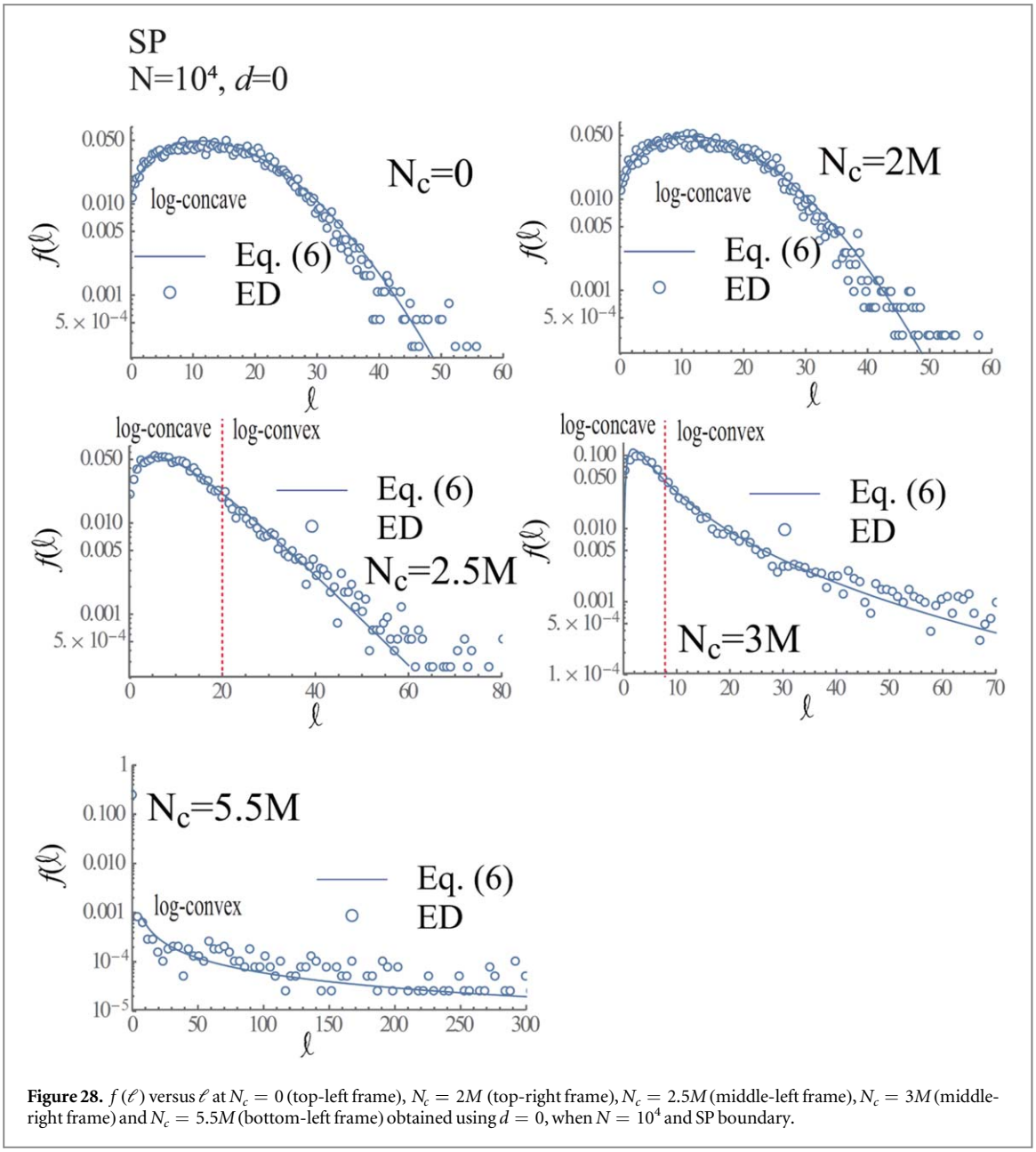

Figure 28. $f(\ell)$ versus ℓ at $N_c = 0$ (top-left frame), $N_c = 2M$ (top-right frame), $N_c = 2.5M$ (middle-left frame), $N_c = 3M$ (middle-right frame) and $N_c = 5.5M$ (bottom-left frame) obtained using $d = 0$, when $N = 10^4$ and SP boundary.

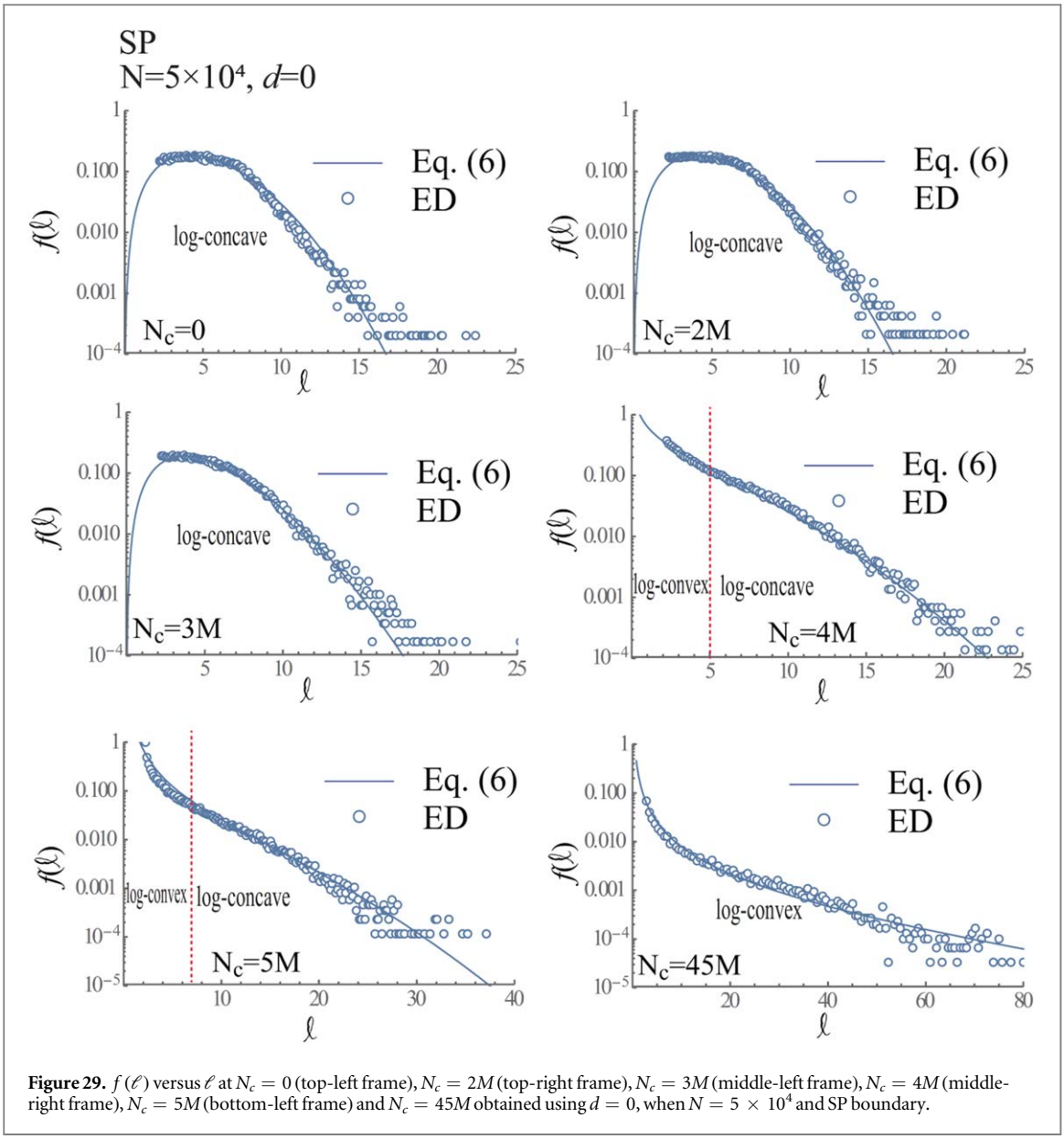

Figure 29. $f(\ell)$ versus ℓ at $N_c = 0$ (top-left frame), $N_c = 2M$ (top-right frame), $N_c = 3M$ (middle-left frame), $N_c = 4M$ (middle-right frame), $N_c = 5M$ (bottom-left frame) and $N_c = 45M$ obtained using $d = 0$, when $N = 5 \times 10^4$ and SP boundary.

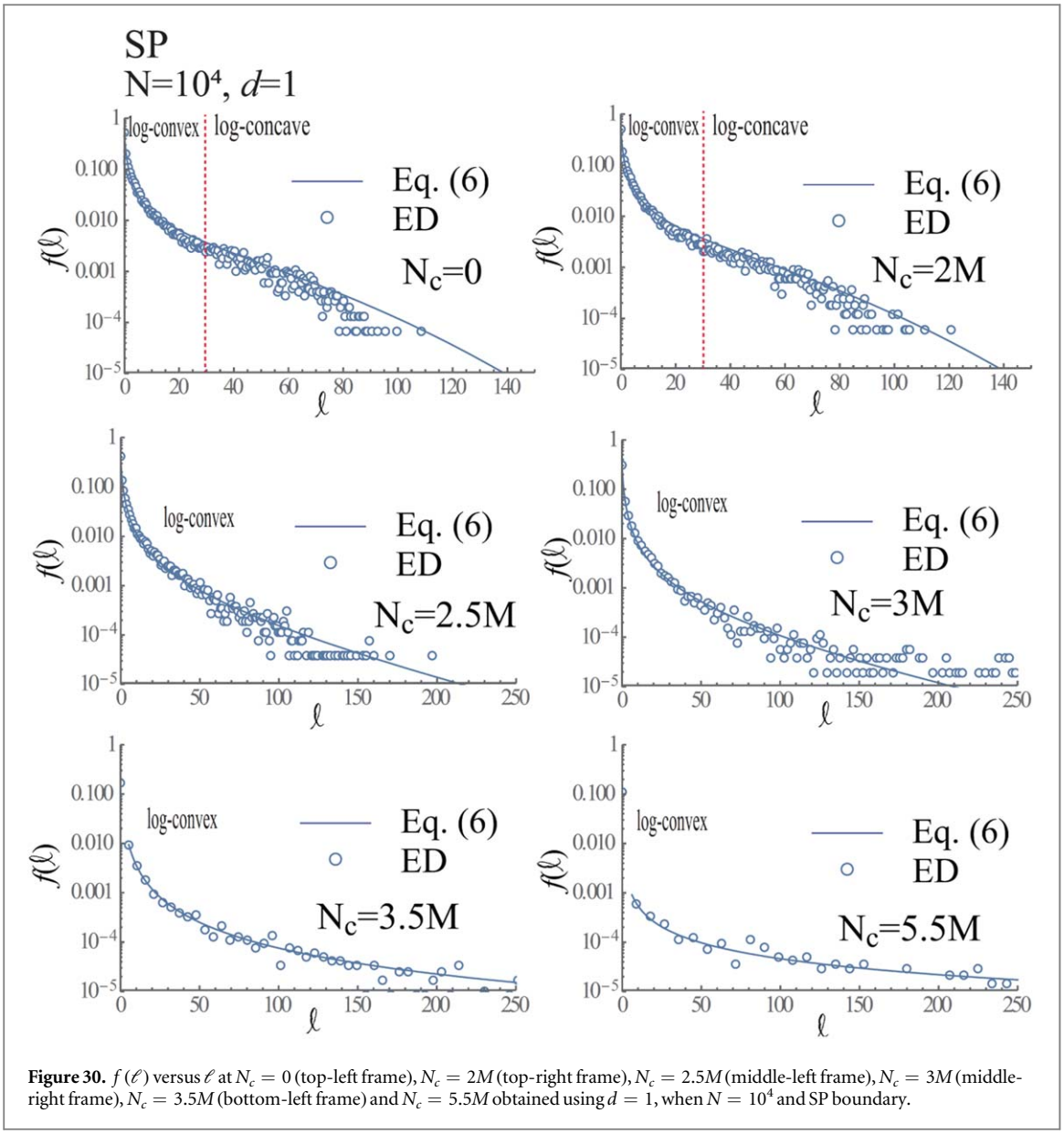

Figure 30. $f(\ell)$ versus ℓ at $N_c = 0$ (top-left frame), $N_c = 2M$ (top-right frame), $N_c = 2.5M$ (middle-left frame), $N_c = 3M$ (middle-right frame), $N_c = 3.5M$ (bottom-left frame) and $N_c = 5.5M$ obtained using $d = 1$, when $N = 10^4$ and SP boundary.

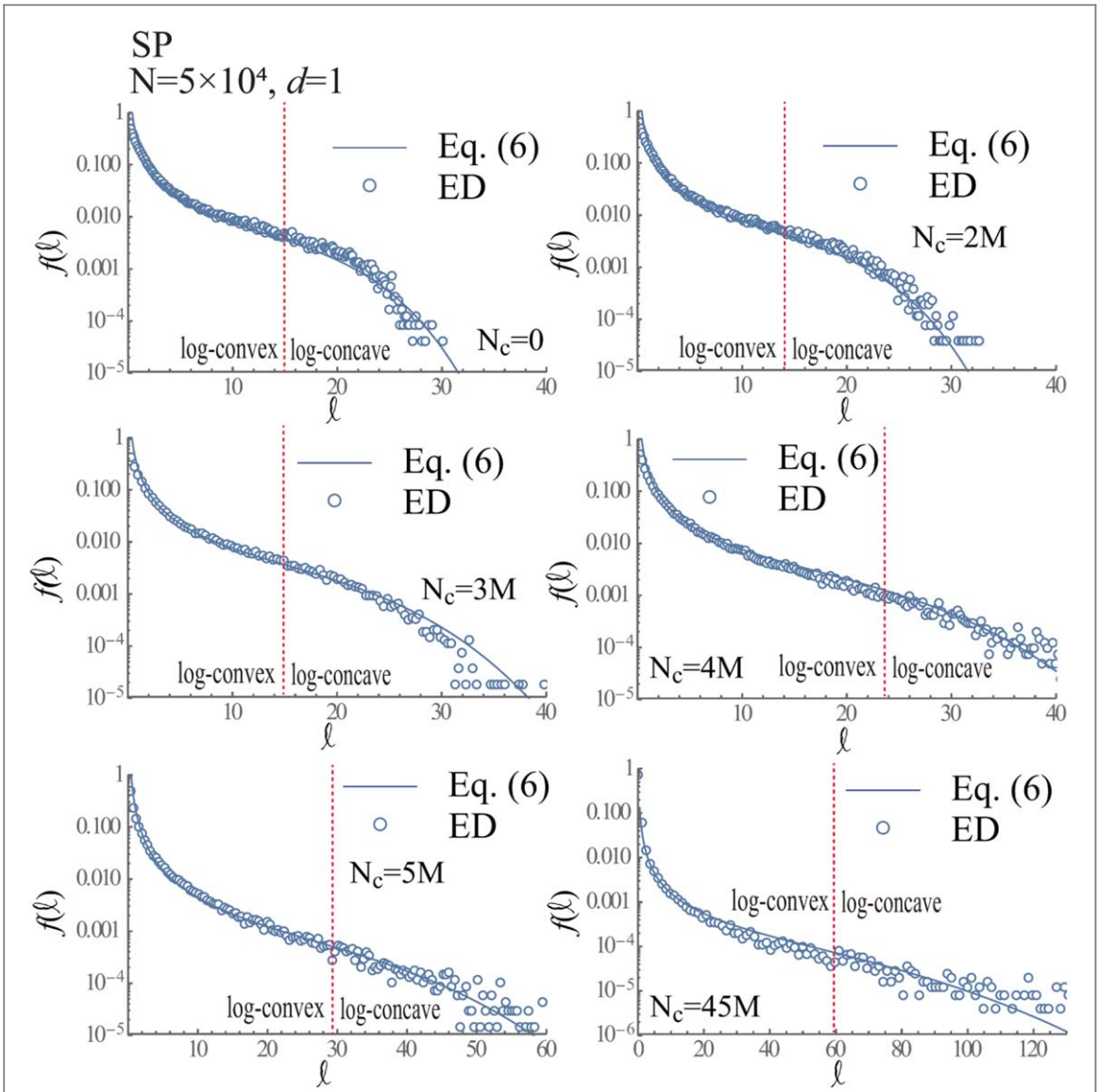

Figure 31. $f(\ell)$ versus ℓ at $N_c = 0$ (top-left frame), $N_c = 2M$ (top-right frame), $N_c = 3M$ (middle-left frame), $N_c = 4M$ (middle-right frame), $N_c = 5M$ (bottom-left frame) and $N_c = 45M$ obtained using $d = 1$, when $N = 5 \times 10^4$ and SP boundary.

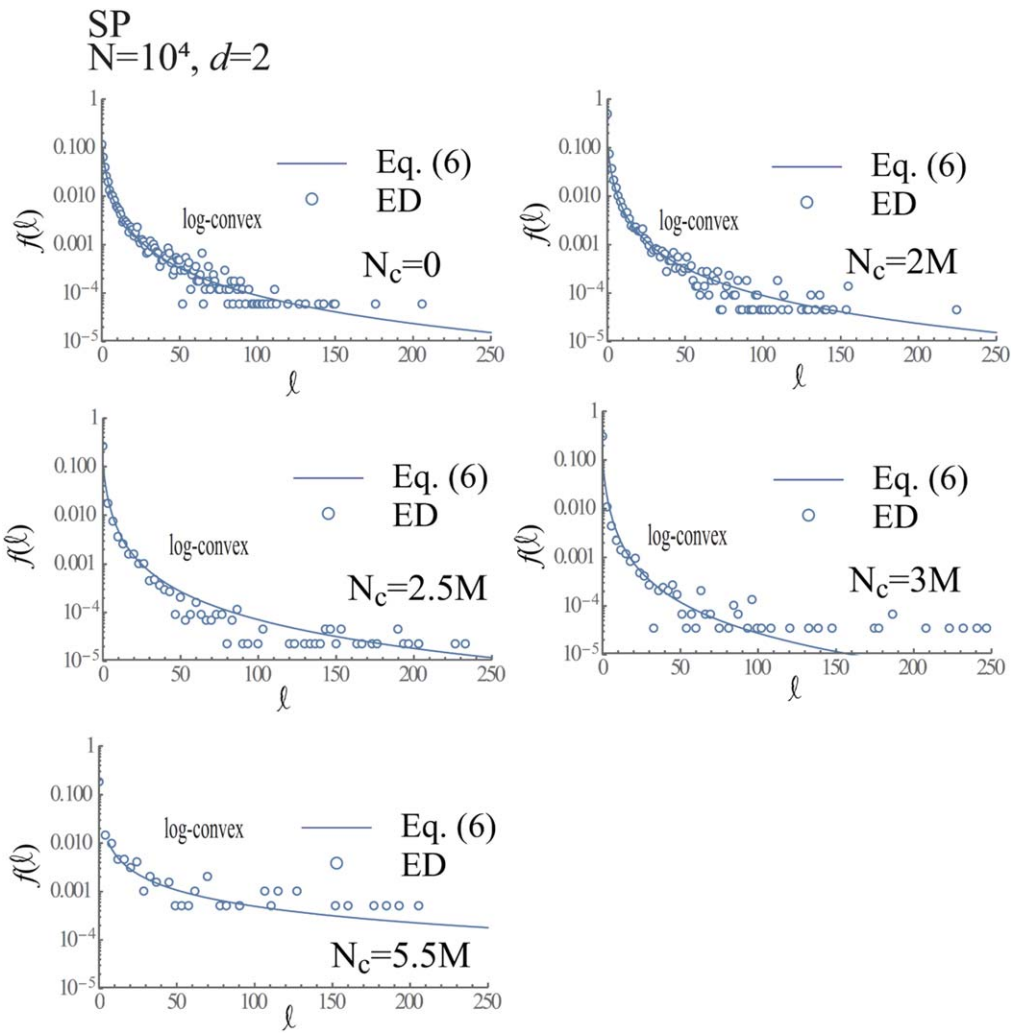

Figure 32. $f(\ell)$ versus ℓ at $N_c = 0$ (top-left frame), $N_c = 2M$ (top-right frame), $N_c = 2.5M$ (middle-left frame), $N_c = 3M$ (middle-right frame) and $N_c = 5.5M$ (bottom-left frame) obtained using $d = 2$, when $N = 10^4$ and SP boundary.

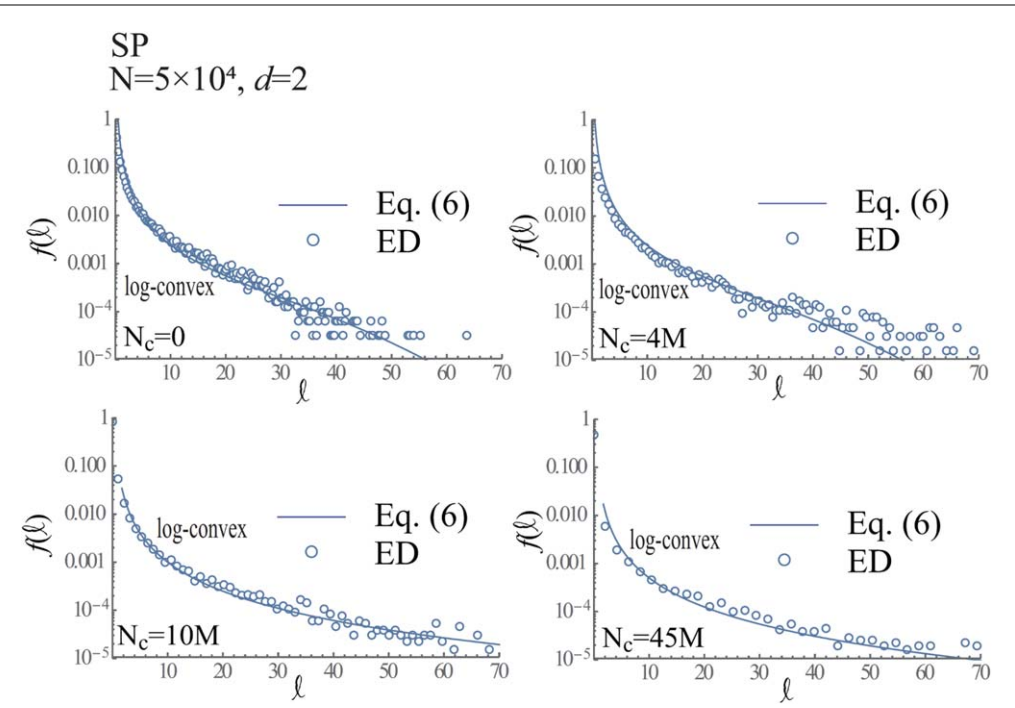

Figure 33. $f(\ell)$ versus ℓ at $N_c = 0$ (upper-left frame), $N_c = 4M$ (upper-right frame), $N_c = 10M$ (lower-left frame) and $N_c = 45M$ (lower-right frame) obtained using $d = 2$, when $N = 5 \times 10^4$ and SP boundary.

Table 3. $\mathfrak{A}$, $\mathfrak{B}$, $\mathfrak{C}$, $\mathfrak{D}$, $\mathfrak{E}$, n and m in equation (6) and corresponding number of the figure, when $d = 0, 1$ and $2, N = 10^4$ and 5×10^4 and SP boundary are used.

Form	d	N	N_c	$\mathfrak{A}$	$\mathfrak{B}$	$\mathfrak{C}$	$\mathfrak{D}$	$\mathfrak{E}$	n	m	figure No.
SP	0	10^4	0	0.012	0.003	1	0.8	1	2	0.75	Figure 28
SP	0	10^4	2M	0.012	0.003	1	0.8	1	2	0.75	Figure 28
SP	0	10^4	2.5M	0.02	0.003	1	0.8	1	0.95	1	Figure 28
SP	0	10^4	3M	5×10^7	18	−1	1	0	2	0.15	Figure 28
SP	0	10^4	5.5M	1	0	0	1	−614	1	0.77	Figure 28
SP	1	10^4	0	1	2.25×10^{-4}	0	3.6	1.83	2	−1.15	Figure 30
SP	1	10^4	2M	1	2.25×10^{-4}	0	3.6	1.83	2	−1.15	Figure 30
SP	1	10^4	2.5M	1	0.015	0	2.46	1.98	1	−1.32	Figure 30
SP	1	10^4	3M	1	0.012	0	2.33	2.26	1	−1.45	Figure 30
SP	1	10^4	3.5M	1	0.1	0	2.13	2.75	1	−1.77	Figure 30
SP	1	10^4	5.5M	1	0	0	107	7.88	1	−1.08	Figure 30
SP	2	10^4	0	1	0	0	1.16	2.9	1	−1.95	Figure 32
SP	2	10^4	2M	1	0	0	1.16	2.9	1	−1.95	Figure 32
SP	2	10^4	2.5M	1	0	0	1.16	2.9	1	−2	Figure 32
SP	2	10^4	3M	1	0	0	1.16	2.9	1	−2.2	Figure 32
SP	2	10^4	5.5M	1	0	0	9.33	4.64	1	−1.1	Figure 32
SP	0	5×10^4	0	1	1.62×10^{-9}	−48	1	0	5.5	2	Figure 29
SP	0	5×10^4	2M	1	2.1×10^{-8}	−42.3	1	0	5	2	Figure 29
SP	0	5×10^4	3M	1	1.66×10^{-2}	−12.3	1	0	2	2	Figure 29
SP	0	5×10^4	4M	1	8.8×10^{-3}	-6,15	1	0	2	0.6	Figure 29
SP	0	5×10^4	5M	1	4.2×10^{-3}	−0.144	1	0	2.5	−1.8	Figure 29
SP	0	5×10^4	45M	1	2.44×10^{-2}	−2.13	1	0	1	−1.5	Figure 29
SP	1	5×10^4	0	0.25	10^{-7}	−3	1	0	5	−1.5	Figure 31
SP	1	5×10^4	2M	0.25	10^{-7}	−3	1	0	5	−1.5	Figure 31
SP	1	5×10^4	3M	0.25	1.6×10^{-6}	−3	1	0	4	−1.5	Figure 31
SP	1	5×10^4	4M	0.25	2.5×10^{-6}	−3	1	0	3.75	−1.5	Figure 31
SP	1	5×10^4	5M	0.25	2.5×10^{-6}	−1	1	0	3.5	−1.75	Figure 31
SP	1	5×10^4	45M	0.25	5×10^{-6}	−1	1	0	2.75	−1.5	Figure 31
SP	2	5×10^4	0	0.25	10^{-5}	−3	1	0	3	−2	Figure 33
SP	2	5×10^4	4M	0.25	10^{-5}	−3	1	0	3	−2	Figure 33
SP	2	5×10^4	10M	0.1	10^{-5}	−3	1	0	3	−2	Figure 33
SP	2	5×10^4	45M	0.1	10^{-5}	−3	1	0	3	−2	Figure 33

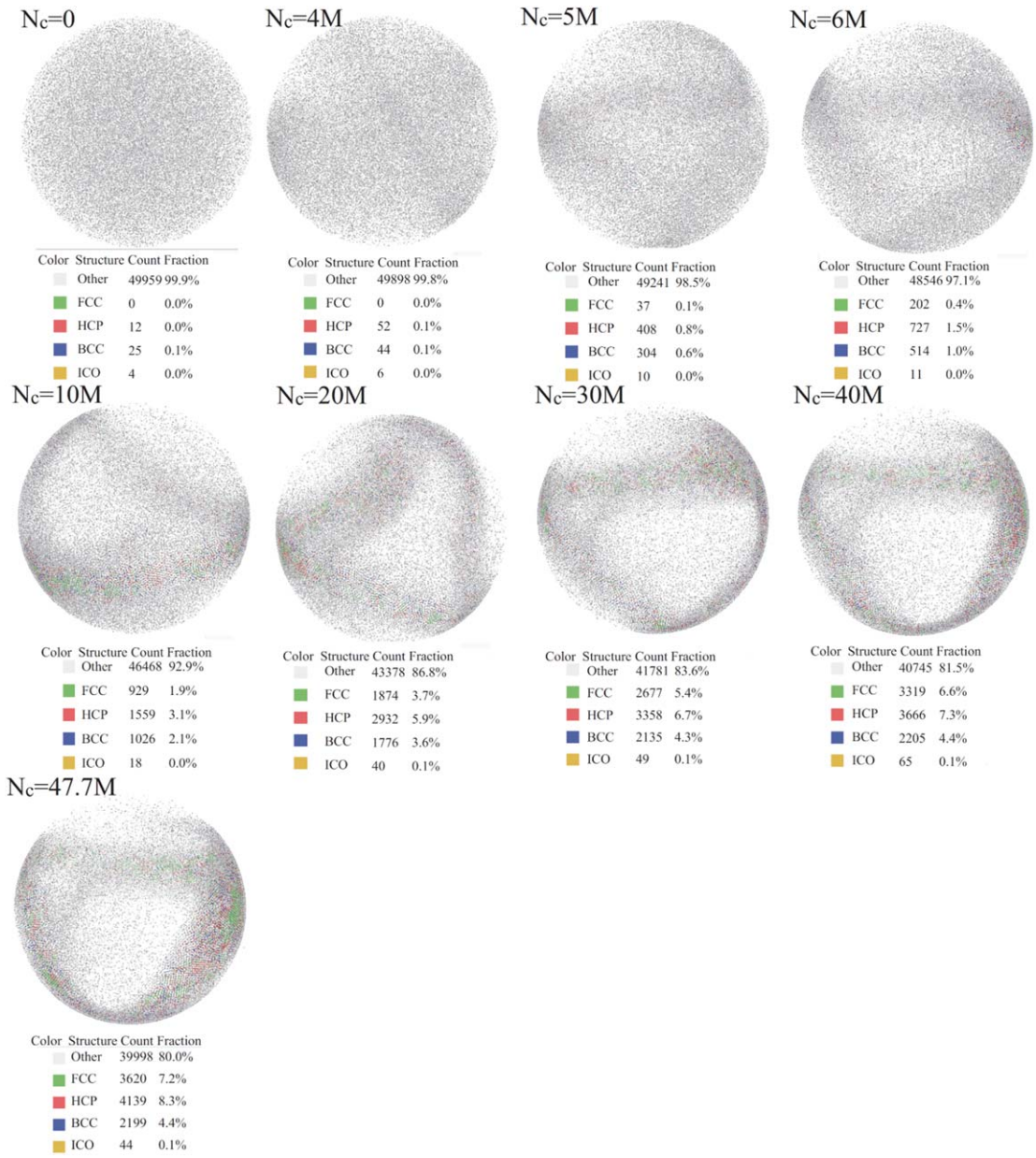

Figure 34. Snapshots of categorized coordination per a granular particle and its fraction obtained using BAA at $N_c = 0, 4M, 5M, 6M, 10M, 20M, 30M, 40M$ and $47.4M$, when $N = 5 \times 10^4$.

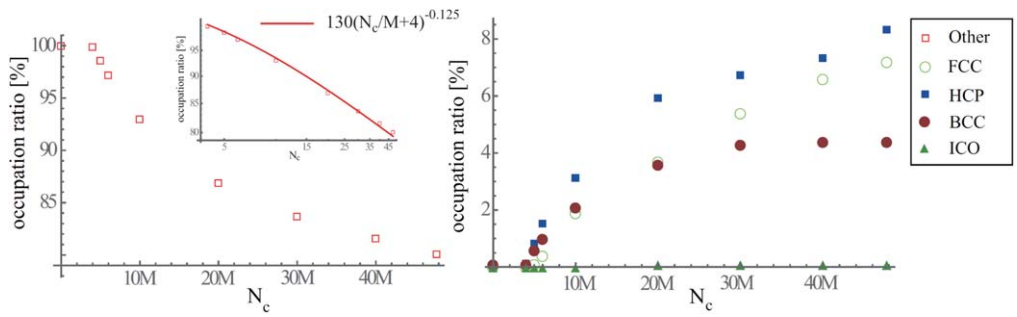

Figure 35. Fractions of categories of coordination versus N_c obtained using BAA (*Other*: left frame, FCC, HCP, BCC and ICO: right frame).

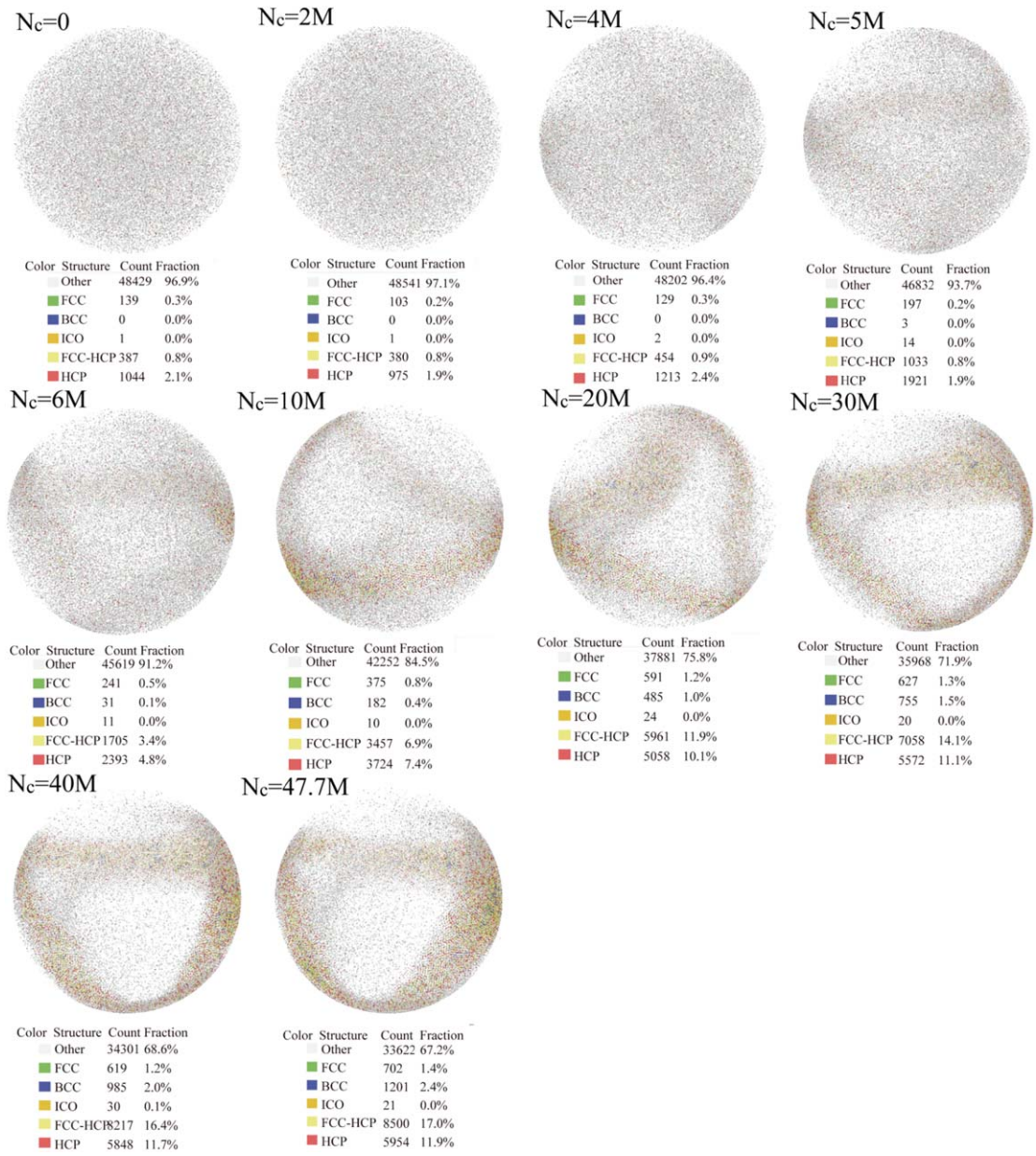

Figure 36. Snapshots of classification of granular gases obtained using VA analysis at $N_c = 0$, $2M$, $4M$, $5M$, $6M$, $10M$, $20M$, $30M$, $40M$ and $47.4M$, when $N = 5 \times 10^4$.

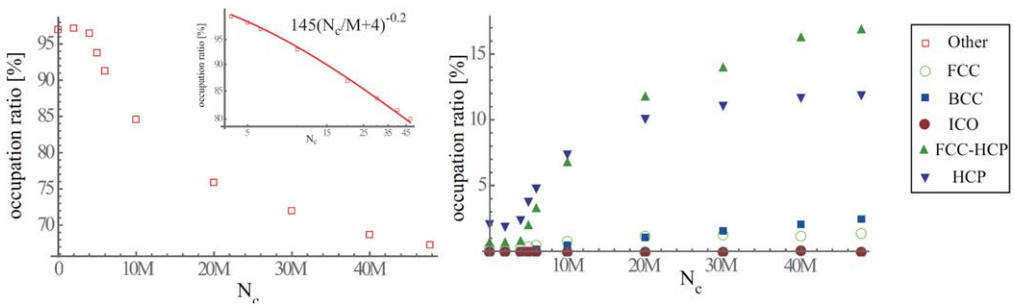

Figure 37. Fractions of categories versus N_c obtained using VA (*Other*: left frame, FCC, HCP, ICO, FCC-HCP and SC: right frame).

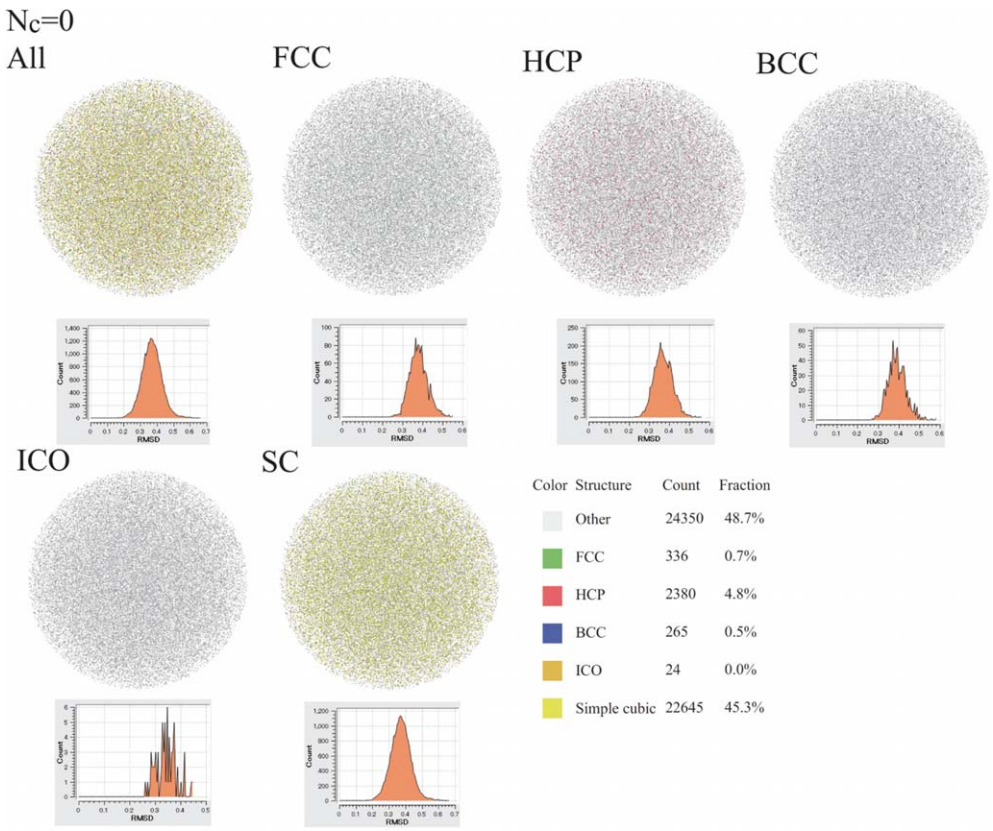

Figure 38. Snapshots of fractions of all categories, *Other*+HCC, *Other*+HCP, *Other*+BCC, *Other*+ICO, and *Other*+SC and their Root-Mean-Square-Deviation (RMSD) distributions at $N_c = 0$ obtained using PTM.

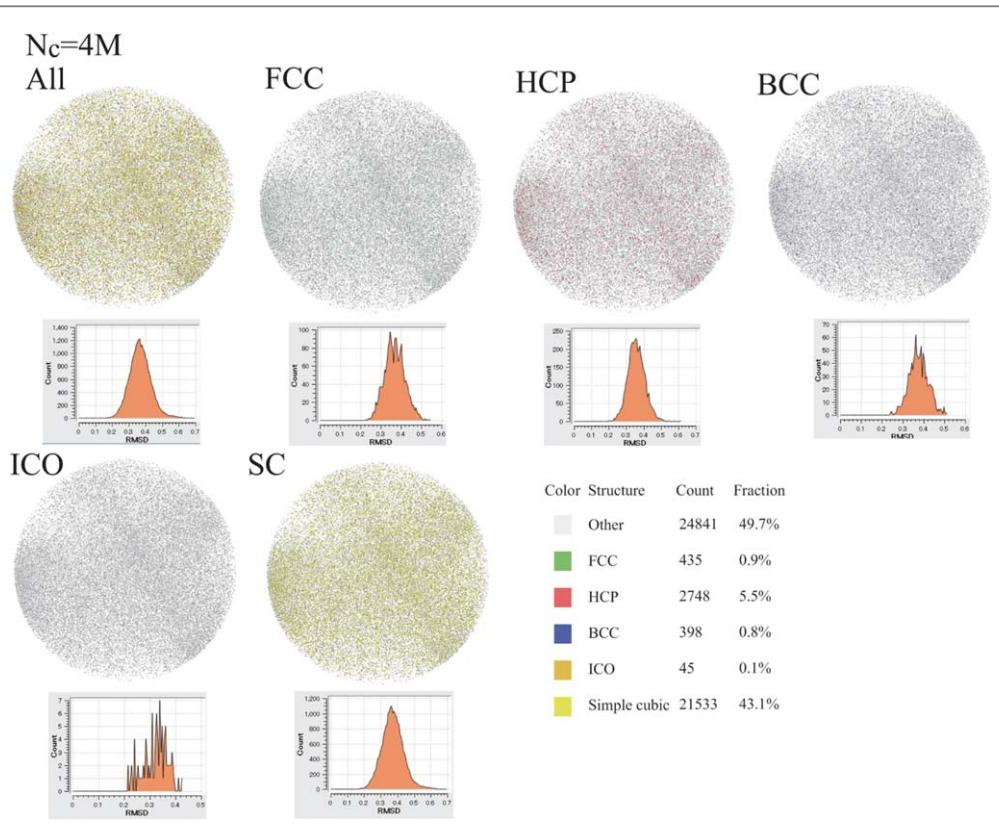

Figure 39. Snapshots of fractions of all categories, *Other*+HCC, *Other*+HCP, *Other*+BCC, *Other*+ICO, and *Other*+SC and their Root-Mean-Square-Deviation (RMSD) distributions at $N_c = 4M$ obtained using PTM.

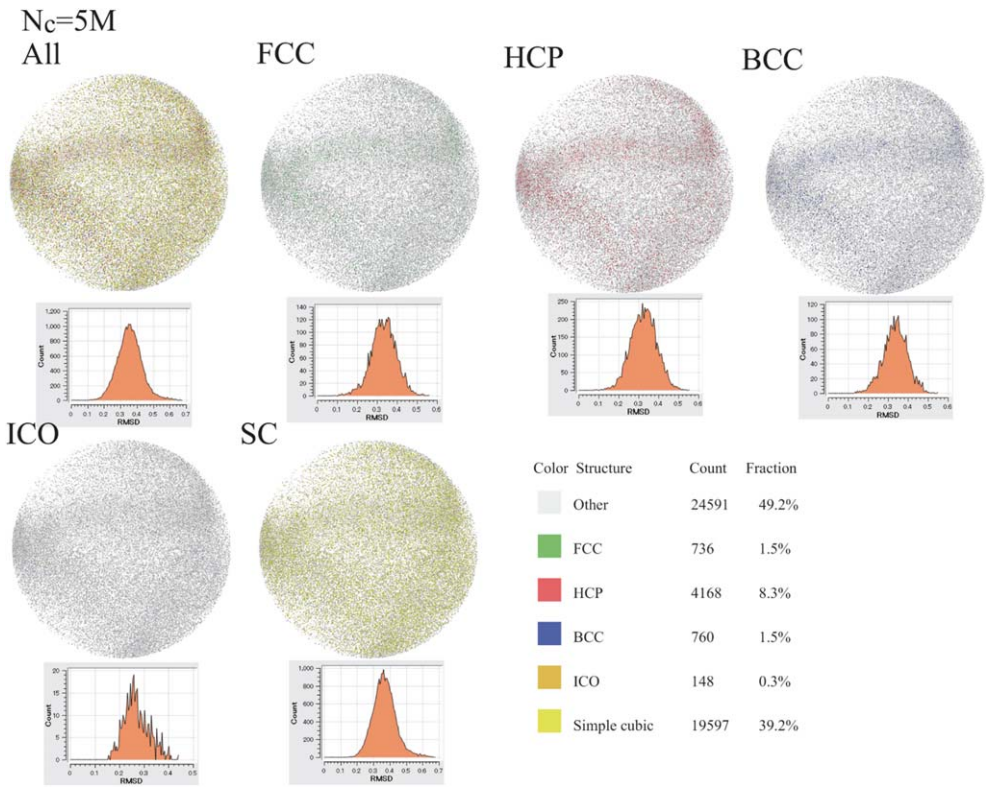

Figure 40. Snapshots of fractions of all categories, *Other*+HCC, *Other*+HCP, *Other*+BCC, *Other*+ICO, and *Other*+SC and their Root-Mean-Square-Deviation (RMSD) distributions at $N_c = 5M$ obtained using PTM.

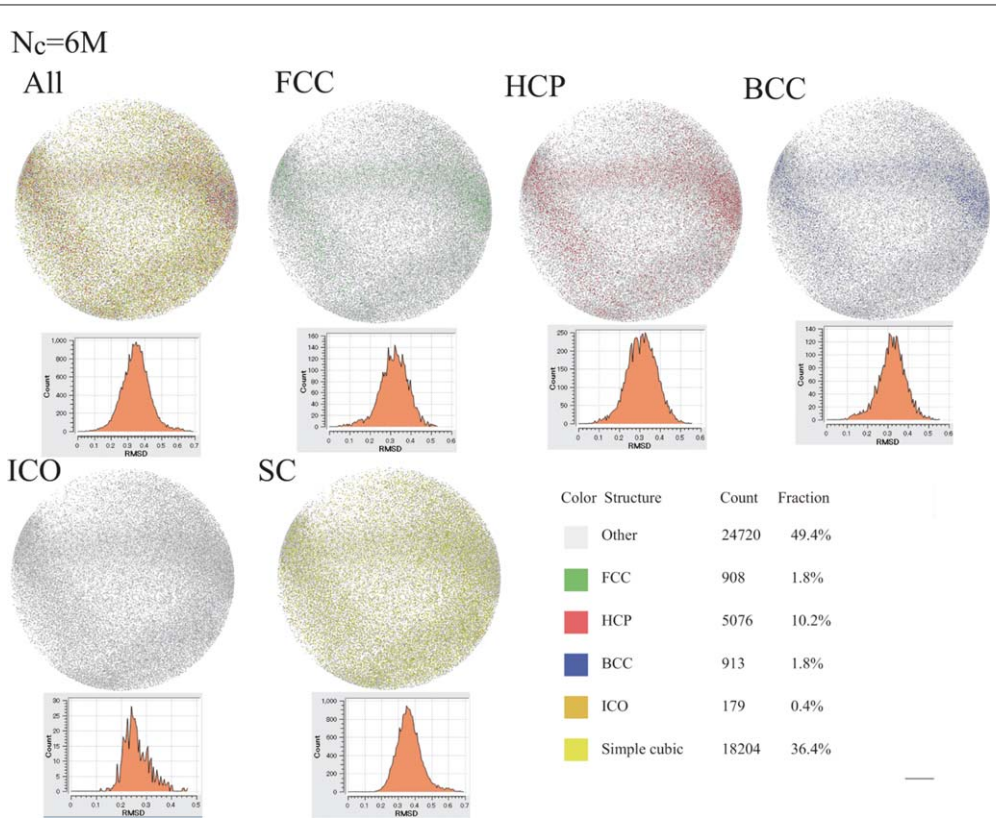

Figure 41. Snapshots of fractions of all categories, *Other*+HCC, *Other*+HCP, *Other*+BCC, *Other*+ICO, and *Other*+SC and their Root-Mean-Square-Deviation (RMSD) distributions at $N_c = 6M$ obtained using PTM.

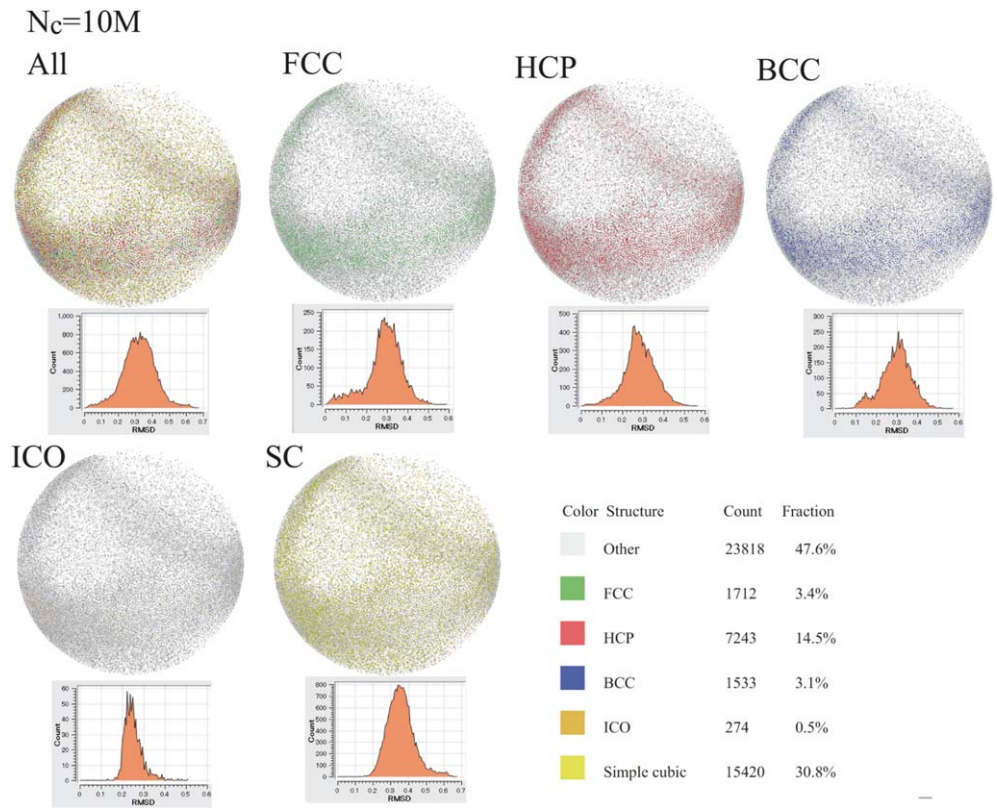

Figure 42. Snapshots of fractions of all categories, *Other*+HCC, *Other*+HCP, *Other*+BCC, *Other*+ICO, and *Other*+SC and their Root-Mean-Square-Deviation (RMSD) distributions at $N_c = 10M$ obtained using PTM.

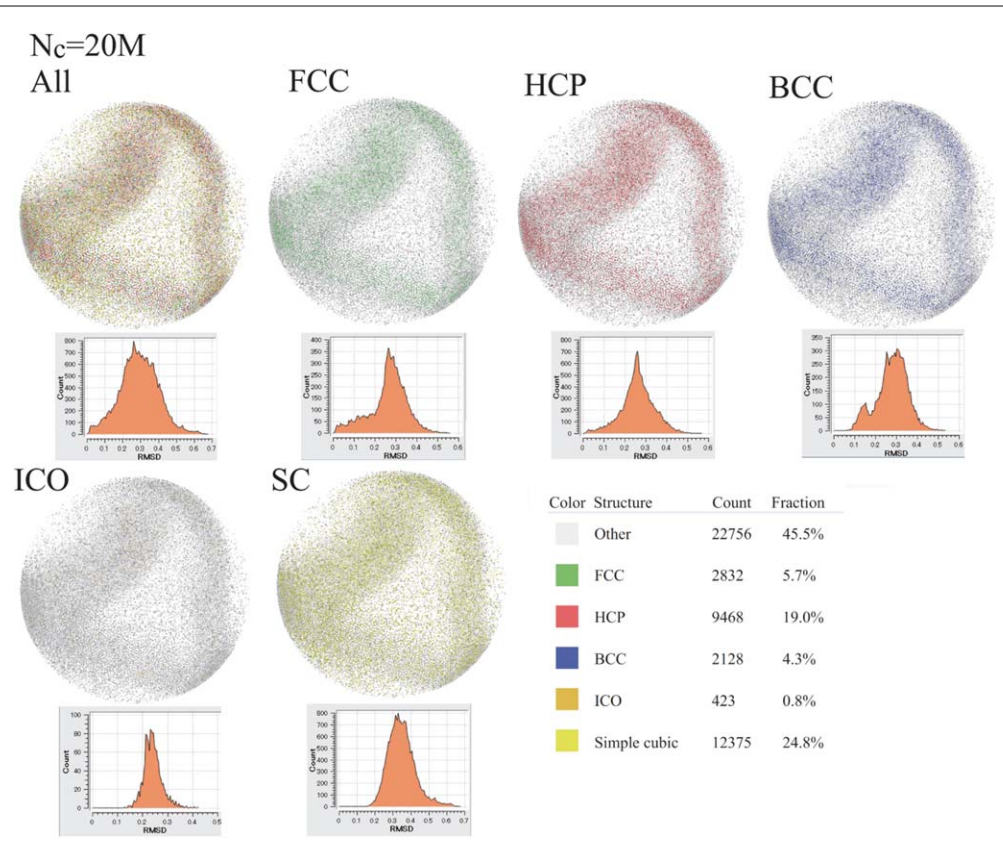

Figure 43. Snapshots of fractions of all categories, *Other*+HCC, *Other*+HCP, *Other*+BCC, *Other*+ICO, and *Other*+SC and their Root-Mean-Square-Deviation (RMSD) distributions at $N_c = 20M$ obtained using PTM.

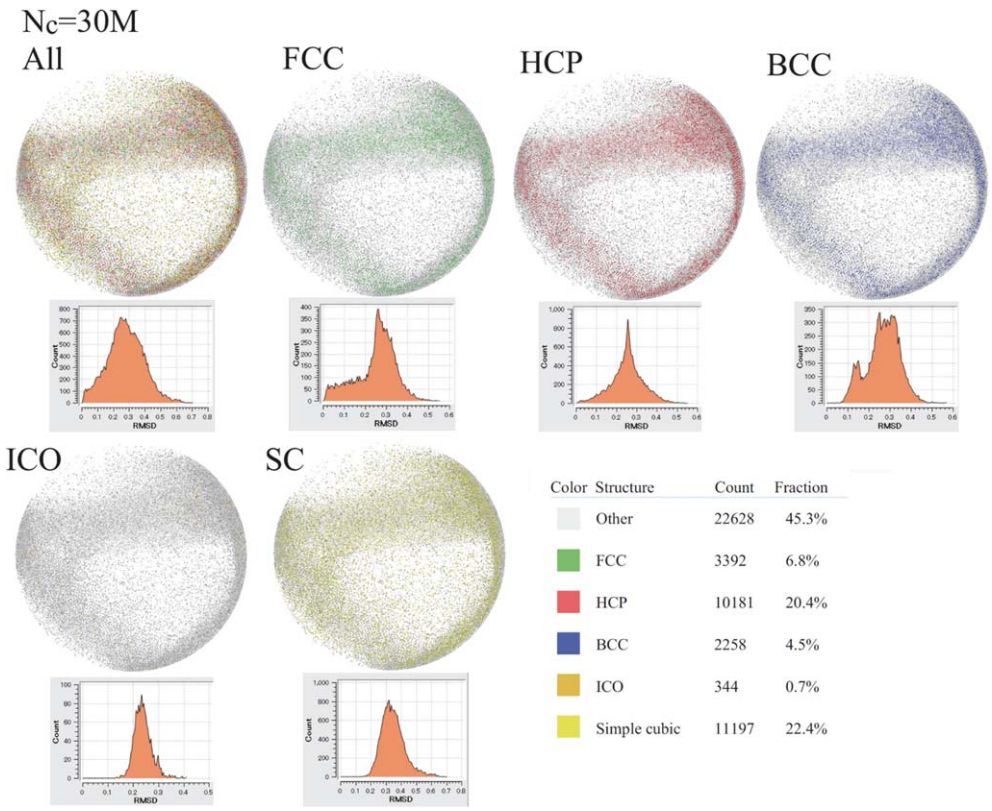

Figure 44. Snapshots of fractions of all categories, *Other*+HCC, *Other*+HCP, *Other*+BCC, *Other*+ICO, and *Other*+SC and their Root-Mean-Square-Deviation (RMSD) distributions at $N_c = 30M$ obtained using PTM.

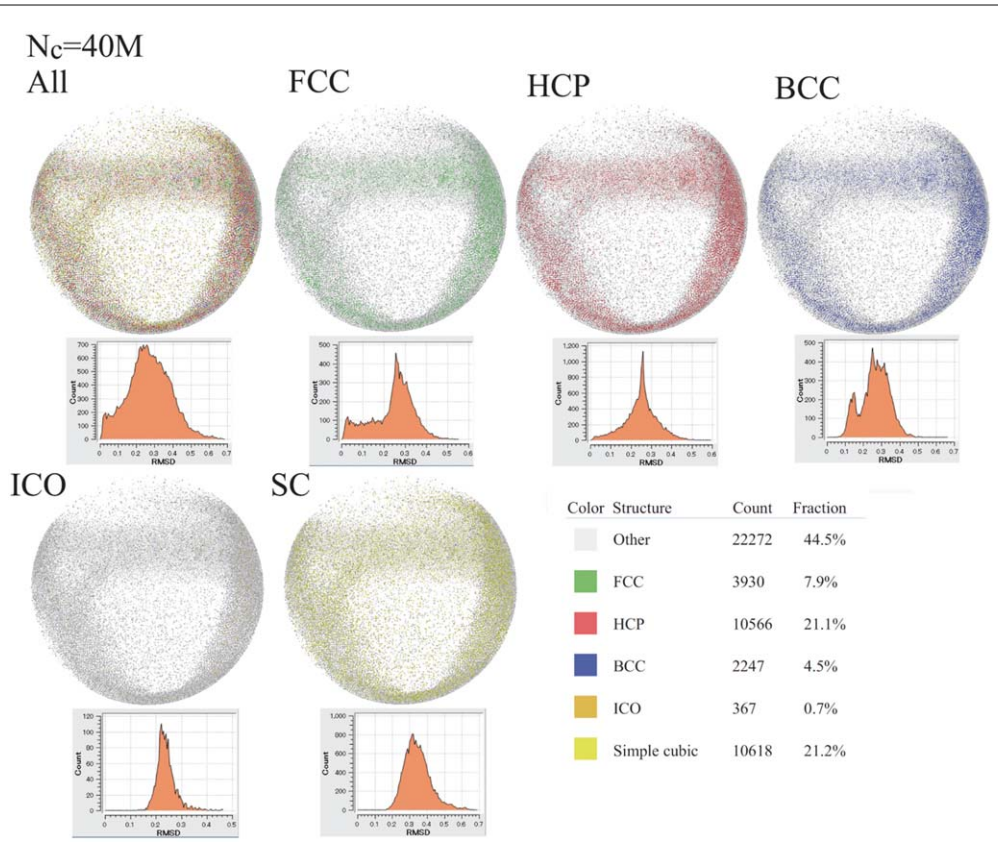

Figure 45. Snapshots of fractions of all categories, *Other*+HCC, *Other*+HCP, *Other*+BCC, *Other*+ICO, and *Other*+SC and their Root-Mean-Square-Deviation distributions (RMSD) at $N_c = 40M$ obtained using PTM.

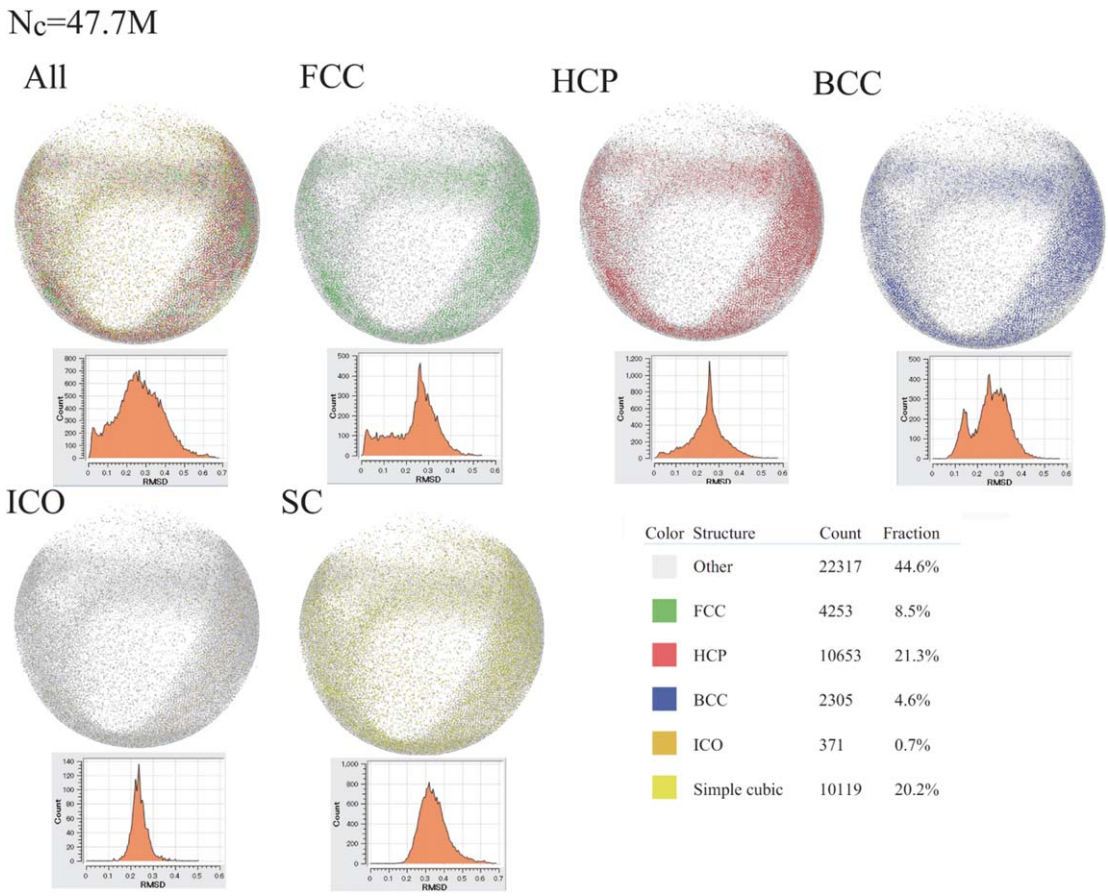

Figure 46. Snapshots of fractions of all categories, *Other*+HCC, *Other*+HCP, *Other*+BCC, *Other*+ICO, and *Other*+SC and their Root-Mean-Square-Deviation (RMSD) distributions at $N_c = 47.7M$ obtained using PTM.

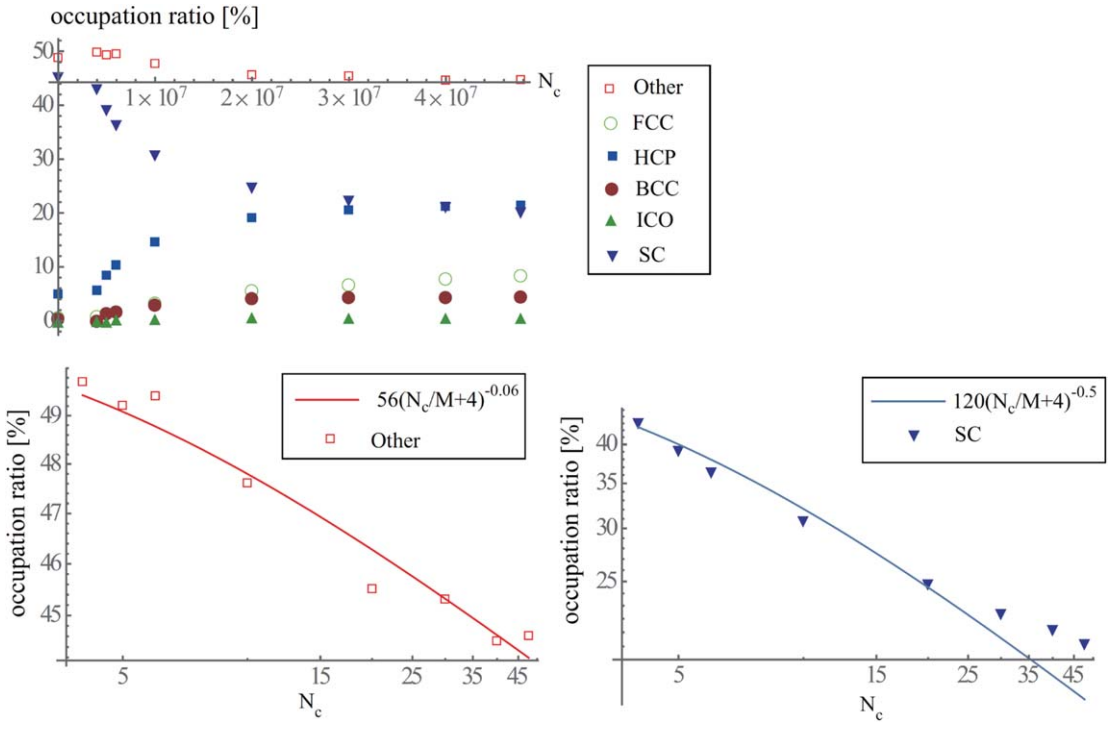

Figure 47. Fractions of categories versus N_c obtained using PTM analysis (top-left frame frame). Log-Log plot of fraction of category *Other* versus N_c together with its fitting function (line) in bottom-left frame and Log-Log plot of fraction of category SC versus N_c together with its fitting function (line) in bottom-right frame.

with the inverse-power-law functions, namely, $56(N_c/M + 4)^{-0.06}$ and $120(N_c/M + 4)^{-0.5}$, respectively. The deviations from the inverse-power-law functions become marked at $N_c \geqslant 30$M in the case of the SC.

5. Concluding remarks

We investigated the transition from the homogeneous cooling state (HCS) to the pattern formation of the granular gases confined by the elastic wall using the topological analyses, namely, PH, BAA, VA and PTM. The topological phase-transition is successfully identified by the switch of the life-span-distribution (lsd) between the log-concave and log-convex, when the dimension of homology is zero and unity in the cases of the SQ and CI boundaries or zero in the case of the SP boundary. The zeroth and first order Betti numbers obtained using the SQ boundary indicate that three topological phases exist, whereas the zeroth and first order Betti numbers obtained using the CI boundary indicate that only two topological phases exist. The analyses of coordination of granular spheres on the basis of the BAA, VA and PTM indicate that the time-evolution of fractions of categories also become standard to judge the topological phase-transition as well as the switch of the lsd between the log-concave and log-convex. The HCP coordination is dominant, when the condensed granular spheres around the wall are categorized as the structured coordination after the adequate time passes by. Finally, we confirmed that these topological analyses, which have been applied to crystal or glass, are also useful for the consideration of the phase-transition of the granular gases.

Acknowledgments

The authors acknowledge the professor Takahito Kashiwabara (Graduate school of Mathematical Science, University of Tokyo, Japan) for his helpful comments on the specific of *homcloud* and professor Andrés Santos (Departamento de Fsica, Universidad de Extremadura, Spain) for his helpful comments on the rotation of cluster of granular particles along the wall.

Appendix A. Simplicial complex

The notion of *simplicial complex* [33] is a generalization of both of polygons and polyhedrons with triangle faces. It is combinatorially constructed by gluing some basic geometric objects called *simplices*. For a non-negative integer p, the *p-simplex* is formally given by a subspace of $\mathbb{R}^{p+1}$ formed by $(t_0, t_1, \cdots, t_p)$ such that $t_0 + t_1 + \cdots t_p = 1$. In the literature, a subspace of a Euclidean space which is linearly isomorphic to the above p-simplex is also called a p-simplex. For example, the notions of 0-simplices, 1-simplices, 2-simplices and 3-simplices coincide with those of points, line segments, triangles and tetrahedrons respectively. We note that polygons are constructed by gluing some line segments along their boundaries in a proper way. Likewise, polyhedrons with triangle faces are constructed by gluing some triangles along their boundaries in a proper way. Then the notion of simplicial complex is defined by a geometric object which is combinatorially constructed by gluing some simplices.

Appendix B. Homology

The p-th Betti number is defined via the *p-th homology theory*. The p-th homology theory is, roughly speaking, the vector space formally generated by p-dimensional holes. We refer the readers to Hatcher's book [20] for exact definitions. The p-th homology theory of a simplicial complex X is usually denoted by $H_p(X; \mathbb{R})$ or $H_p(X)$. For example, if we write by X the simplicial complex in figure 3, then the p-th homology theory $H_p(X)$ is calculated to be a 1-dimensional vector space for $p = 0$ and 2-dimensional vector space for $p = 1$ as we give a heuristic discussion in the previous subsection. Moreover, the p-th homology theory $H_p(X)$ is a 0-dimensional vector space for $p \geqslant 2$.

The p-th Betti number is *defined* by the dimension of the vector space $H_p(X)$. Since the homology theory is based on vector spaces not on numbers as the Betti number, it becomes possible to deal with linear homomorphisms between them. It makes us to obtain more rich information about given simplicial complexes than the Betti number does.

Appendix C. Persistent homology

The *p-th persistent homology* is, formally speaking, the persistence module induced by a filtration of a simplicial complex. For the convenience of the readers, we unpack the definition as follows. The p-th persistent homology of a filtration X_t of a simplicial complex X is given by the following data,

- A sequence of vector spaces $M_t = H_p(X_t)$ where H_p denotes the p-th homology theory. See section B.
- A family of linear homomorphisms, $f_{t_0,t_1}: M_{t_0} \to M_{t_1}$ for $t_0 < t_1$ such that $f_{t_1,t_2} \circ f_{t_0,t_1} = f_{t_0,t_2}$ for $t_0 < t_1 < t_2$. It is induced by the inclusion maps $X_{t_0} \to X_{t_1}$.

Note that we deal with finite simplicial complexes so that each vector space M_t is finite-dimensional. A persistence module with finite-dimensional components is called to be pointwise finite-dimensional. By Crawley-Boevey [34], any pointwise finite-dimensional persistence module is a direct sum of *interval modules*. An interval module is a persistence module $\{L_t; g_{t_0,t_1}\}$ such that for some interval I in the real line,

$$L_t = \begin{cases} \mathbb{R} & (t \in I) \\ 0 & (t \notin I), \end{cases}$$

and

$$g_{t_0,t_1} = \begin{cases} id_{\mathbb{R}} & (t_0,\, t_1 \in I) \\ 0 & (\text{otherwise}). \end{cases}$$

For the p-th persistent homology $\{M_t; f_{t_0,t_1}\}$ of a filtration, we can take a decomposition of interval modules by Crawley-Boevey. Let $\{L_t; g_{t_0,t_1}\}$ be an interval module component on an interval I as above. If $a < b$ are endpoints of the interval I, then we say that the p-th dimensional hole is born at $t = a$ and dead at $t = b$. By using an interval module decomposition, we obtain the PD.

ORCID iDs

Ryosuke Yano https://orcid.org/0000-0003-1682-6117

References

[1] Onuki A 2002 *Phase Transition Dynamics* (Cambridge: Cambridge University Press) (https://doi.org/10.1017/CBO9780511534874)
[2] Henkel M *et al* (ed) 2007 *Ageing and the Glass Transition* (*Lecture Notes in Physics* vol 716) (Berlin: Springer) (https://doi.org/10.1007/3-540-69684-9)
[3] Okabe A *et al* 2009 *Spatial Tessellations: Concepts and Applications of Voronoi Diagrams* vol 501 (New York: Wiley) (https://doi.org/978-0-471-98635-5)
[4] Edelsbrunner H and Harer J 2010 *Computational Topology: An Introduction* (Berline-Heidelberg: Springer) (https://doi.org/10.1007/978-3-540-33259-6_7)
[5] Nakamura T *et al* 2015 Persistent homology and many-body atomic structure for medium-range order in the glass *Nanotech* **26** 304001
[6] Bi D *et al* 2011 Jamming by shear *Nature* **480** 355
[7] Kramar M *et al* 2013 Persistence of force networks in compressed granular media *Phys. Rev.* E **87** 042207
[8] Brilliantov N V and Pöschel T 2010 *Kinetic Theory of Granular Gases* (Oxford: Oxford University Press) 9780199588138
[9] Miller S and Luding S 2004 Cluster growth in two-and three-dimensional granular gases *Phys. Rev.* E **69** 031305
[10] Brey J J *et al* 2016 Stability analysis of the homogeneous hydrodynamics of a model for a confined granular gas *Phys. Rev.* E **93** 062907
[11] Santos A 2003 Transport coefficients of d-dimensional inelastic Maxwell models *Physica* A **321** 442–66
Santos A, Kremer G M and dos Santos M 2011 Sonine approximation for collisional moments of granular gases of inelastic rough spheres *Phys. Fluids* **23** 030604
[12] Yano R 2013 Transport coefficients of the inelastic variable hard sphere *J. Phys.* A **46** 375502
[13] Esipov S E and Pöschel T 1997 The granular phase diagram *J. Stat. phys.* **86** 1385–95
[14] Ackland G J and Jones A P 2006 Applications of local crystal structure measures in experiment and simulation *Phys. Rev.* B **73** 054104
[15] Larsen P M, Schmidt S and Schiøtz J 2016 Robust structural identification via polyhedral template matching *Modell. and Simul. in Mat. Sci. and Eng.* **24** 055007
[16] Grossman E L, Zhou T and Ben-Naim E 1997 Towards granular hydrodynamics in two dimensions *Phys. Rev.* E **55** 4200
[17] Pöschel T and Schwager T 2005 *Computational Granular Dynamics: Models and Algorithms* (Berlin-Heidelberg: Springer) (https://doi.org/10.1007/3-540-27720-X)
[18] Kondic L *et al* 2012 Topology of force networks in compressed granular media *EPL* **97** 54001
[19] Ichinomiya T, Obayashi I and Hiraoka Y 2017 Persistent homology analysis of craze formation *Phys. Rev.* E **95** 012504
[20] Hatcher A 2005 *Algebraic Topology* (Cambridge: Cambridge University Press)
[21] Mischaikow K. *et al* (http://chomp.rutgers.edu/Projects/Computational_Homology/OriginalCHomP/software/intro.php)
[22] Edelsbrunner H 2010 Alpha shapes—a survey *Tessellations in the Sci.* **27** 1–25
[23] Zomorodian A 2012 Topological data analysis *Advan. in Appl. and Compu. Topo.* **70** 1–39
[24] Rycroft C 2009 VORO++: A three-dimensional Voronoi cell library in C++ *Chaos* **19** 041111
[25] Lazar E.A (https://www.seas.upenn.edu/ mlazar/VoroTop/)

[26] Stukowski A 2009 Visualization and analysis of atomistic simulation data with OVITO-the open visualization tool *Modell. and Simul. in Mate. Sci. and Eng.* **18** 015012
[27] Weinberg L 1966 A simple and efficient algorithm for determining isomorphism of planar triply connected graphs *IEEE Trans. Circuit Theory* **13** 142–8
[28] Honeycutt J D and Andersen H C 1978 Molecular dynamics study of melting and freezing of small Lennard-Jones clusters *J. Phys. Chem.* **91** 4950–63
[29] Horn B K P 1987 Closed-form solution of absolute orientation using unit quaternions *J. Opt. Soc. Am.*, A **4** 629–42
[30] Theobald D L 2005 Rapid calculation of RMSDs using a quaternion-based characteristic polynomial *Acta Crystallogr*, A **61** 478–80
[31] Hernandez-Ortiz J P, Stoltz C G and Graham M D 2005 Transport and collective dynamics in suspensions of confined swimming particles *Phys. Rev. Lett.* **95** 204501
[32] Obayashi I *et al* (https://www.wpi-aimr.tohoku.ac.jp/hiraoka_labo/homcloud/)
[33] In this paper, we only consider finite simplicial complexes whereas infinite simplicial complexes can be defined and studied in a careful way.
[34] Crawley-Boevey W 2015 Decomposition of pointwise finite-dimensional persistence modules *J. Algebra and its Appl.* **14** 1550066